Using Support Vector Machines, Convolutional Neural Networks and Deep Belief Networks for Partially Occluded Object Recognition

Joseph Lin Chu

A Thesis

in

The Department

of

Computer Science

Presented in Partial Fulfillment of the Requirements

for the Degree of Master of Computer Science (Computer Science) at

Concordia University

Montréal, Québec, Canada

March 2014

CONCORDIA UNIVERSITY

School of Graduate Studies

This is to certify that the thesis prepared

By: **Joseph Lin Chu**

Entitled: **Using Support Vector Machines, Convolutional Neural Networks and Deep Belief Networks for Partially Occluded Object Recognition**

and submitted in partial fulfilment of the requirements for the degree of

Master of Computer Science

complies with the regulations of this University and meets the accepted standards with respect to originality and quality.

Signed by the final examining committee:

_____ Dr. Rajagopalan Jayakumar, Chair

_____ Dr. Tien Dai Bui, Examiner

_____ Dr. Thomas G. Fevens, Examiner

_____ Dr. Adam Krzyżak, Supervisor

Approved by _____

Chair of CS Department or Graduate Program Director

_____ 2014 _____

Dean of Faculty

Abstract

Using Support Vector Machines, Convolutional Neural Networks and Deep Belief Networks for Partially Occluded Object Recognition

Joseph Lin Chu

Artificial neural networks have been widely used for machine learning tasks such as object recognition. Recent developments have made use of biologically inspired architectures, such as the Convolutional Neural Network, and the Deep Belief Network. A theoretical method for estimating the optimal number of feature maps for a Convolutional Neural Network maps using the dimensions of the receptive field or convolutional kernel is proposed. Empirical experiments are performed that show that the method works to an extent for extremely small receptive fields, but doesn't generalize as clearly to all receptive field sizes. We then test the hypothesis that generative models such as the Deep Belief Network should perform better on occluded object recognition tasks than purely discriminative models such as Convolutional Neural Networks. We find that the data does not support this hypothesis when the generative models are run in a partially discriminative manner. We also find that the use of Gaussian visible units in a Deep Belief Network trained on occluded image data allows it to also learn to classify non-occluded images.

Acknowledgement

I would like to heartily thank my supervisor, Professor Adam Krzyżak, for allowing me to be his graduate student and helping and supporting me greatly in my efforts to conduct research and become a Master of Computer Science. I want to thank him for his patience, generosity, and consideration.

I would also like to thank my friends and family for their support and advice. In particular, I want to thank my mother and father for their dedicated support and their willingness to allow me to explore the thesis option and pursue my dreams to be a researcher in this field. I want to thank them for their patience and their ever loyal support. As well, thank you my friends for listening to me, and supporting me throughout this endeavour.

I would like as well to thank Concordia University, and the good people at the Department of Computer Science and Software Engineering, for enabling me to pursue my dreams and achieve this much. I especially want to thank Halina Monkiewicz for her assistance as graduate coordinator in getting me into those courses that mattered.

In addition I wish to thank Professor Doina Precup of McGill University for letting me take her class and learn a great deal from her. I would also like to thank Professor Ching Y. Suen, Professor Sabine Bergler, Professor Tien Dai Bui, and Professor Thomas G. Fevens of Concordia University for also letting me take their classes and allowing me to learn from them, as well as any other professors and fellow students who I was granted the pleasure of becoming acquainted with in my journey through graduate school.

Thank you dear reader for taking the time to look at the culmination of years of effort, struggle, and uncertainty. I hope that you enjoy the fruits of my labour.

Table of Contents

List of Figures

List of Tables

List of Algorithms

List of Symbols

$\langle\rangle$	angle brackets - enclose the expectations of the distribution labeled in the subscript
$*$	convolution - integral of the product of two functions after one is reversed and shifted

List of Abbreviations

AI	Artificial Intelligence
ANN	Artificial Neural Network
CDBN	Convolutional Deep Belief Network
CK	Cohn-Kanade
CNN	Convolutional Neural Network
CRBM	Convolutional Restricted Boltzmann Machine
CRUM	Computational-Representational Understanding of Mind
CUDA	Compute Unified Device Architecture
DBM	Deep Boltzmann Machine
DBN	Deep Belief Network
GPU	Graphical Processing Unit
LIRBM	Local Impact Restricted Boltzmann Machine
MSE	Mean Squared Error
PDP	Parallel Distributed Processing
RBM	Restricted Boltzmann Machine
SML	Stochastic Maximum Likelihood
SVM	Support Vector Machine
TCNN	Tiled Convolutional Neural Network
TFD	Toronto Face Database

Chapter 1

Introduction

Artificial Intelligence (AI) is a field of computer science that is primarily concerned with mimicking or duplicating human and animal intelligence in computers. This is often considered a lofty goal, as the nature of the human mind has historically been seen as something beyond scientific purview. From Plato to Descartes, philosophers generally believed the mind to exist in a separate realm of ideas and souls, a world beyond scrutiny by the natural sciences.

In the 20th century however, psychology gradually began to show that the mind was within the realm of the natural [41]. Cognitive Science in particular has embraced functionalism, the view that mental states can exist anywhere that the functionality exists to represent them, and the Computational-Representational Understanding of Mind (CRUM) [53], which suggests that the brain can be understood with analogy to computational models. This includes using what are known as connectionist models, which attempt to duplicate the biological structure of the brains neuronal networks. And in the past few decades, many strides have been made in the field of AI, and much of this has come from developments in machine learning and pattern recognition.

Machine Learning is a particular subfield of AI that attempts to get computers to learn much in the way that the human brain is capable of doing. As such, research into machine learning generally involves developing learning algorithms that are able to perform such tasks as object recognition or speech recognition. Object recognition is of particular interest to the Cognitive Scientist in that it shows potential to allow for a semantic representation of objects to be realized.

Psychologists have long debated about the nature of mental imagery [2, p. 111]. Though the idea that images are stored in the mind as mental pictures, of the brain being able to exactly reproduce visual perception in all its original detail is thought of as an incorrect understanding of perception, it does appear that brain is able to recollect constructed representations of objects perceived previously [42]. These representations lack the exact pixel by pixel accuracy of the originating visual object, but then it is highly unlikely that our perception of images possesses such accuracy either. The phenomenon of visual illusions is only possible because perception fundamentally involves a degree of cognitive processing.

What we see in our minds is not merely a reflection of the real world so much as a combination of real world information with prior knowledge of a given object or objects in general. The properties of objects we see are thus partly projections of our memory, filling in the blanks and allowing us to identify objects without having to thoroughly investigate every angle. For these reasons we have chosen to study occluded images in particular, as they better represent what humans in the real world see. It is the hope that machine learning algorithms can be applied to learn to recognize objects even though they may be obscured by occlusions in the visual field.

Among the most successful of the machine learning algorithms are those used with Artificial Neural Networks (ANNs), which are biologically inspired connectionist computational constructs of potentially remarkable sophistication and value. Based loosely upon the actual biological structure of neuronal networks in the brain, research into ANNs has

had a long and varied history. As a machine learning algorithm, ANNs have historically suffered from significant challenges and setbacks due the limitations of hardware at the time, as well as mistaken beliefs about the limits of their algorithmic potential. Only recently have computers reached the level of processing speed for the use of ANN to be realistically feasible.

ANNs can range in complexity from a single node Perceptron, to a multilayer network with thousands of nodes and connections. The early Perceptron was famously denigrated by Marvin Minsky as being unable to process the exclusive-or circuit, and much ANN research funding was lost after such criticisms [47]. And yet, after many years in the AI Winters of the 1970s, late 1980s, and early 1990s where funding for AI research dried up temporarily, ANNs have seen a recent resurgence of popularity.

The most recent resurgence owes a great deal to two major developments in the field of ANNs. The first was the development of various types of feed-forward, that is, non-cyclical, networks that used a localized branching structural architecture first proposed by Fukushima in the Neocognitron [19], but popularized practically by LeCun with the Convolutional Neural Network (CNN) [29] seen in Figure 1.1. The CNN was, when it first came out, astonishingly successful at image recognition compared to previous ANNs.

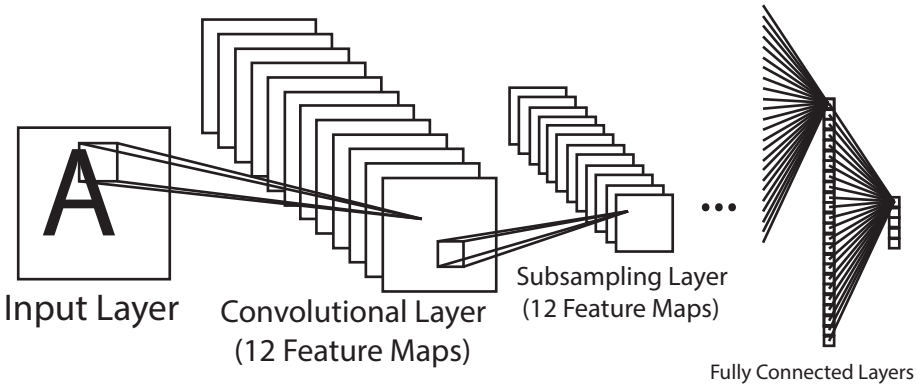

Figure 1.1: The basic architecture of the CNN.

The second development was the Deep Belief Network (DBN), and the Restricted Boltzmann Machine (RBM) that made up the elements of the DBN, by Hinton at the University of Toronto [23]. The DBN and RBM essentially put recurrent ANNs, that is, ANNs with cyclical connections, back on the map, by providing a fast learning algorithm for recurrent ANNs that showed promise on many tasks.

The CNN and the DBN together form two pillars of the Deep Learning movement in ANN research. The CNN was marvelous for its time because it essentially took its inspiration from the biological structure of the visual cortex of the human and animal brain. The visual cortex is arranged in such a manner as to be highly hierarchical, with many layers of neurons. It also has very localized receptive fields for various neurons. This deep architecture was difficult to duplicate with traditional ANNs, so the CNN famously hard-wired it into the structure of the network itself. It made the Backpropagation algorithm, which had previously had severe difficulties with deep hierarchies, a useful algorithm again. The DBN solved a particular problem that had plagued its earlier forefather, the Boltzmann Machine, by using RBMs that had their lateral connections removed as seen in Figure 1.2 and Figure 1.3. This greatly simplified the task of calculating the energy function of the RBM, and enabled it to be quickly computed in comparison to a regular Boltzmann Machine.

Recently there has been a proliferation of new research using both techniques. In fact, there have even been attempts to combine the techniques into a Convolutional Deep Belief Network (CDBN) [31]. The results have shown dramatic performance gains in the field of image recognition.

Traditional CNNs are feed-forward neural networks, while DBNs make use of RBMs that use recurrent connections. The fundamental difference between these networks then, is that the DBN is capable of functioning as a generative model, whereas a CNN is merely a discriminative model. A generative model is able to model all variables probabilistically

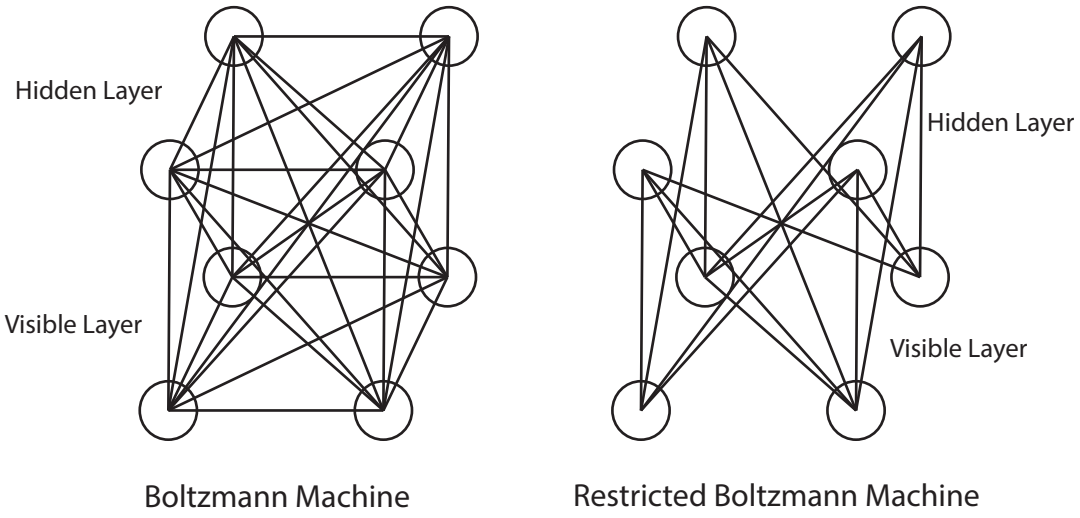

Figure 1.2: The structure of the general Boltzmann Machine, and the RBM.

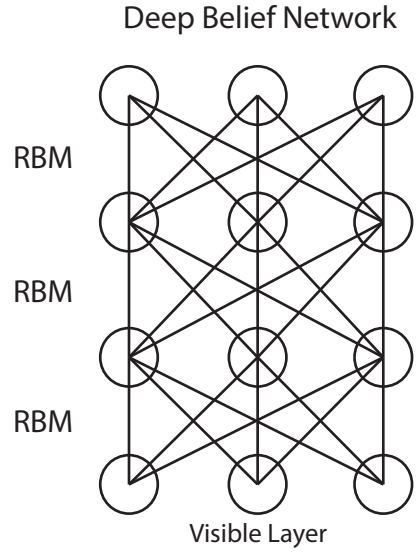

Figure 1.3: The structure of the DBN.

and therefore to generate values for any of these variables. In that sense it can do things like reproduce samples of the original input. A discriminative model on the other hand models only the dependence of an unobserved variable on an observed variable, which is sufficient to perform classification or prediction tasks, but which cannot reproduce samples like a generative model can. This suggests that DBNs should perform better on the task of occluded object recognition, as they ought to be able to use their generative effects to

partially reconstruct the image to aid in classification. This is what we wish to show in our work comparing CNNs, and DBNs [9].

Such research has a myriad of potential applications. In addition to the aforementioned potential to realize object representations in an artificial mind, a more immediate and realistic goal is to advance reverse image search to a level of respectable performance at identifying objects from user provided pictures. For instance, a user could provide an image with various objects, some of which may well be occluded by other objects, and a program could potentially identify and classify the various objects in the image. There are a wide variety of potential uses for a system that is able to effectively identify objects despite occlusions, as real world images are rarely uncluttered and clean of occlusion.

Object recognition is not the only area of research that stands to benefit from improved machine learning algorithms. Speech recognition has also benefited recently from the use of these algorithms [36]. As such, it's apparent that advances in ANNs have a wide variety of applications in many fields. In terms of the applicability of our research on occlusions, speech is also known to occasionally have their own equivalent to occlusions in the form of noise. Being able to learn effectively in spite of noise, whether visual noise like occlusions, or auditory noise, is an essential part of any real-world pattern recognition system. Perceptual noise will exist in any of the perceptual modalities, whether visual, auditory, or somatosensory. Missing data, occlusions, noise, these things are common concerns in any signal processing system. Therefore, the value of this research potentially extends beyond mere object recognition. Nevertheless, for simplicity's sake, we shall focus on the object recognition problem, and the particular problem of occlusions as a region of particular interest.

Chapter 2

Literature Review

2.1 Basics of Artificial Neural Networks

ANNs have their foundation in the works of McCulloch and Pitts [33], who presented the earliest models of the artificial neuron [34]. Among the earliest learning algorithms for such artificial neurons was presented by Hebb [20], who devised Hebbian Learning, which was based on the biological observation that neurons that fired together, tended to wire together, so to speak. The basic foundation of the artificial neuron is simply described by Equation (2.1).

$$output = f(\sum_{i=1}^{n} w_i x_i) = f(net) \tag{2.1}$$

Where, w_i is the connection weight of node i, x_i is the input of node i, and f is the activation function, which is usually a threshold function or a sigmoid function such as

Equation (2.2).

$$f(net) = z + \frac{1}{1 + exp(-x \cdot net + y)} \tag{2.2}$$

Then the Perceptron model was developed by Rosenblatt [45], which used a gradient descent based learning algorithm. The Perceptron is centred on a single neuron, and can be considered the most basic of feed-forward ANNs. They are able to function as linear classifiers, using a simple step function as seen in Equation (2.3).

$$f(net) = \begin{cases} 1 & \text{if } \sum_{i=0}^{n} w_i x_i > 0 \\ 0 & \text{otherwise} \end{cases} \tag{2.3}$$

There are some well-known limitations regarding the Perceptron that were detailed by Minsky & Papert [35], namely that they do not work on problems where the sample data are not linearly separable.

Learning algorithms for ANNs containing many neurons were developed by Dreyfus [14], Bryson & Ho [6], Werbos [56], and most famously by McClelland & Rumelhart [32], who revived the concept of ANNs under the banner of Parallel Distributed Processing (PDP). The modern implementation of the Backpropagation learning algorithm was provided by Rumelhart, Hinton, & Williams [46]. Backpropagation was a major advance on traditional gradient descent methods, in that it provided multi-layer feed-forward ANNs with a highly competitive supervised learning algorithm. The Backpropagation algorithm (as shown in Algorithm 1) is a supervised learning algorithm that changes network weights to try to minimize the Mean Squared Error (MSE) (see Equation (2.4)) between the desired and the

actual outputs of the network.

$$MSE = \frac{1}{P}\sum_{p=1}^{P}\sum_{j=1}^{K}(|o_{p,j} - d_{p,j}|)^2 \tag{2.4}$$

Where, $d_{p,j}$ is the desired output, and $o_{p,j}$ is the actual output.

Algorithm 1: The Backpropagation training algorithm. From: [34]

Start with randomly chosen weights;
while *MSE is unsatisfactory and computational bounds are not exceeded,* **do**
  for *each input pattern* x_p, $1 \geq p \geq P$ **do**
    Compute hidden node inputs ($net^{(1)}_{p,j}$);
    Compute hidden node outputs ($x^{(1)}_{p,j}$);
    Compute inputs to the output $nodes(net^{(2)}_{p,k})$;
    Compute the network outputs ($o_{p,k}$);
    Compute the error between $o_{p,k}$ and desired output $d_{p,k}$;
    Modify the weights between hidden and output nodes:;
    $\Delta w^{2,1}_{k,j} = \eta(d_{p,k} - o_{p,k})S'(net^{(2)}_{p,k})x^{(1)}_{p,j}$;
    Modify the weights between input and hidden nodes:;
    $\Delta w^{1,0}_{j,i} = \eta \sum_k \left((d_{p,k} - o_{p,k})S'(net^{(2)}_{p,k})\ w^{(2,1)}_{k,j}\right) S'(net^{(1)}_{p,j})x_{p,i}$;

2.2 Convolutional Neural Networks

The earliest of the hierarchical ANNs based on the visual cortexs architecture was the Neocognitron, first proposed by Fukushima & Miyake [19]. This network was based on the work of neuroscientists Hubel & Wiesel [27], who showed the existence of Simple and Complex Cells in the visual cortex. A Simple Cell responds to excitation and inhibition in a specific region of the visual field. A Complex Cell responds to patterns of excitation and

inhibition in anywhere a larger receptive field. Together these cells effectively perform a delocalization of features in the visual receptive field. Fukushima took the notion of Simple and Complex Cells to create the Neocognitron, which implemented layers of such neurons in a hierarchical architecture [18]. However, the Neocognitron, while promising in theory, had difficulty being put into practice effectively, in part because it was originally proposed in the 1980s when computers simply weren't as fast as they are today.

Then LeCun et al. [29] developed the CNN while working at AT&T labs, which made use of multiple Convolutional and Subsampling layers, while also brilliantly using stochastic gradient descent and backpropagation to create a feed-forward network that performed astonishingly well on image recognition tasks such as the MNIST, which consisted of digit characters. The Convolutional Layer of the CNN is equivalent to the Simple Cell Layer of the Neocognitron, while the Subsampling Layer of the CNN is equivalent to the Complex Cell Layer of the Neocognitron. Essentially they delocalize features from the visual receptive field, allowing such features to be identified with a degree of shift invariance. The differences between these layers can be seen in Figure 2.1.

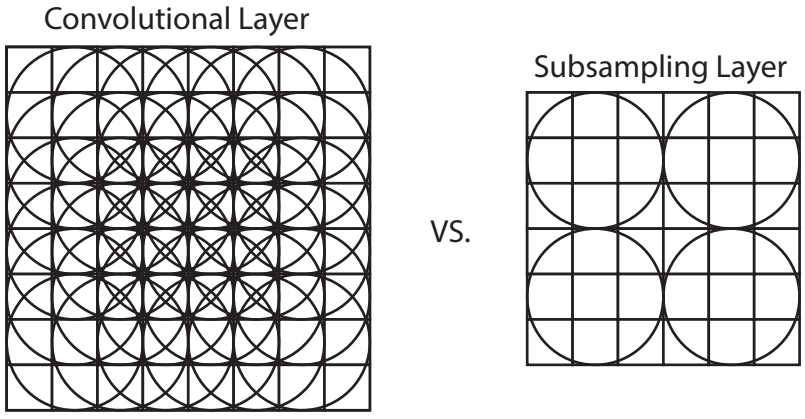

Figure 2.1: A comparison between the Convolutional layer and the Subsampling layer. Circles represent the receptive fields of the cells of the layer subsequent to the one represented by the square lattice. On the left, an 8 x 8 input layer feeds into a 6 x 6 convolutional layer using receptive fields of size 3 x 3 with an offset of 1 cell. On the right, a 6 x 6 input layer feeds into a 2 x 2 subsampling layer using receptive fields of size 3 x 3 with an offset of 3 cells.

This unique structure allows the CNN to have two important advantages over a fully-connected ANN. First, is the use of the local receptive field, and second is weight-sharing. Both of these advantages have the effect of decreasing the number of weight parameters in the network, thereby making computation of these networks easier.

More details regarding the CNN are described in Chapter 3.

2.3 Support Vector Machines

The Support Vector Machine (SVM) is a powerful discriminant classifier first developed by Cortes & Vapnik [13]. Although not considered to be an ANN strictly speaking, Collobert & Bengio [12] showed that they had many similarities to Perceptrons with the obvious exception of learning algorithm. CNNs were found to be excellent feature extractors for other classifiers such as SVMs as seen in Huang & LeCun [26], as well as Ranzato et al. [43]. This generally involves taking the output of the lower layers of the CNN as feature extractors for the classifier.

2.4 Deep Belief Networks

One of the more recent developments in machine learning research has been the Deep Belief Network (DBN). The DBN is a recurrent ANN with undirected connections. Structurally, it is made up of multiple layers of RBMs, such that it can be seen as a "deep architecture". "Deep architectures" can have many hidden layers, as compared to "shallow architectures" which only have usually one hidden layer. To understand how this "deep architecture" is an effective structure, we must first understand the basic nature of a recurrent ANN.

Recurrent ANNs differ from feed-forward ANNs in that their connections can form

cycles. Such networks cannot use simple Backpropagation or other feed-forward based learning algorithms. The advantage of recurrent ANNs is that they can possess associative memory-like behaviour. Early Recurrent ANNs, such as the Hopfield network [25], were limited. The Hopfield network was only a single layer architecture that could only learn very limited problems due to limited memory capacity. A multi-layer generalization of the Hopfield Network was developed known as the Boltzmann Machine [1], which while able to store considerably more memory, suffered from being overly slow to train. A variant of the Boltzmann Machine, which initially saw little use, was first known as a Harmonium [52], but later called a RBM, and was developed by removing the lateral connections from the network. Then Hinton [21] developed a fast algorithm for RBMs called Contrastive Divergence, which uses Gibbs sampling within a gradient descent process. An RBM can be defined by the energy function in Equation (2.5) [3].

$$E(v,h) = \sum_{i \in visible} a_i v_i - \sum_{j \in hidden} b_j h_j - \sum_{i,j} v_i h_j w_{i,j} \tag{2.5}$$

where v_i and h_j are the binary states of the visible unit i and hidden unit j, a_i and b_j are their biases, and $w_{i,j}$ is the weight connection between them [22].

The weight update in an RBM is given by Equation (2.6) below.

$$\Delta w_{i,j} = \epsilon(\langle v_i h_j \rangle_{data} - \langle v_i h_j \rangle_{recon}) \tag{2.6}$$

By stacking RBMs together, they formed the DBN, which produced then state of the art performance on such tasks as the MNIST [23]. Later DBNs were also applied to 3D object recognition [37]. Ranzato, Susskind, Mnih, & Hinton [44] also showed how effective DBNs could be on occluded facial images.

More details of the DBN are provided in Chapter 4.

2.5 Further Developments in Artificial Neural Networks

There has even been a proliferation of work on combining CNNs and DBNs. The CDBN of Lee, Grosse, Ranganath, & Ng [31] combined the two algorithms together. This is possible because strictly speaking the Convolutional nature of the CNN is in the structure of the network, which the DBN can implement. To do this, one creates Convolutional Restricted Boltzmann Machines (CRBMs) for the CDBN to use in its layers. Another modification has also been shown by Schulz, Muller, & Behnke [50], which creates Local Impact Restricted Boltzmann Machines (LIRBMs), which utilize localized lateral connections, similar to work by Osindero & Hinton [40]. These networks are primarily RBMs in terms of learning algorithm, but both utilize CNN style localizing structures.

Deep Boltzmann Machines (DBMs) courtesy of Salakhutdinov & Hinton [48] brought about a dramatic reemergence of the old Boltzmann Machine architecture. Using a new learning algorithm, they were able to produce exceptional results on the MNIST and NORB. Ngiam et al. [38] also developed a superior version of the CNN called the Tiled Convolutional Neural Network (TCNN). Despite these state-of-the-art advances, we choose to use more developed and mature algorithms, namely the SVM, CNN, and DBN.

Chapter 3

Optimizing Convolutional Neural Networks

3.1 Overview

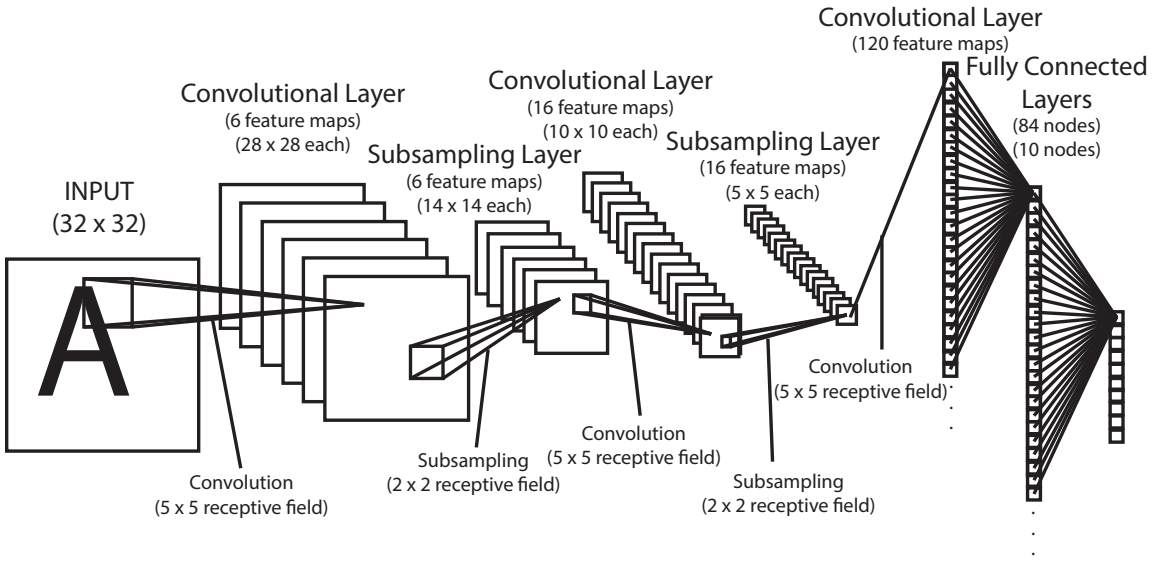

Figure 3.1: The architecture of the LeNet-5 Convolutional Neural Network.

Figure 3.1 shows the entire architecture of the LeNet-5 CNN, as the quintessential example of a CNN [29]. It consists of a series of layers, including an input layer, followed by a number of feature extracting Convolutional and Subsampling layers, and finally a number of fully connected layers that perform the classification.

A Convolutional layer can be described according to:

$$x_{out} = S(\sum_i x_{in} * k_i + b), \tag{3.1}$$

where x_{in} is the previous layer, k is a convolution kernel, S is a non-linear function (such as a hyperbolic tangent sigmoid, described in Equation (3.2)), and b is a scalar bias. See [26] for details.

$$S = \tanh x = \frac{\sinh x}{\cosh x} = \frac{e^x - e^{-x}}{e^x + e^{-x}} = \frac{e^{2x} - 1}{e^{2x} + 1} = \frac{1 - e^{-2x}}{1 + e^{-2x}}. \tag{3.2}$$

This output creates a feature map that is made up of nodes that each effectively share the same weights of a receptive field or convolutional kernel. So, as in the example from Figure 2.1, a 3x3 receptive field applied to an 8x8 input layer will create a 6x6 feature map with 9 weights + 1 bias = 10 free parameters and $9 \times 36 = 324$ weights + 1 bias = 325 connections. The number of free parameters therefore is equal to the number of nodes in the receptive field multiplied by the number of feature maps in the current layer, multiplied by the number of feature maps in the previous layer (the input layer counts as one feature map), plus biases. Meanwhile, the number of total connections is equal to the number of nodes in the receptive field multiplied by the number of nodes in each feature map multiplied by the number of feature maps in the current layer, multiplied by the number of feature maps in the previous layer (the input layer counts as one feature map), plus biases. To train such weights, we can use gradient descent, with the gradient of a shared weight being

the sum of the gradient of the shared parameters.

A Subsampling layer can be described as follows:

$$x_{out} = S(\beta \sum x_{in}^{n \times n} + b), \tag{3.3}$$

where $x_{in}^{n \times n}$ is either the average or the max of an $n \times n$ block in the previous layer, β is a trainable scalar, b is a scalar bias, and S is a non-linear function (such as a hyperbolic tangent sigmoid). See [26] for details.

This output results in a number of subsampled feature maps equal to the number of feature maps of the previous layer. The number of free parameters then is simply the number of feature maps, plus biases. The total number of connections is equal to the number of nodes in the subsampled feature maps multiplied by the number of feature maps multiplied by the number of nodes in the receptive field, plus biases.

Some CNNs also implement non-complete connection schemes between layers, such that only some of the feature maps of a previous layer are connected to the feature maps of a subsequent layer. These can range from hand-crafted connection matrices as seen in [29], to random connection matrices, as well as completely connected implementations.

The final fully connected layers can be a wide variety of ANN classifiers, but are most commonly are a multi-layer perceptron that takes as input the output of the previous feature extracting layers, and performs classification. The entire CNN can be trained with Backpropagation, and that is how we choose to train our networks.

3.2 Topology of LeNet-5

The convolutional operator used in LeNet-5 can be described in more detail as follows:

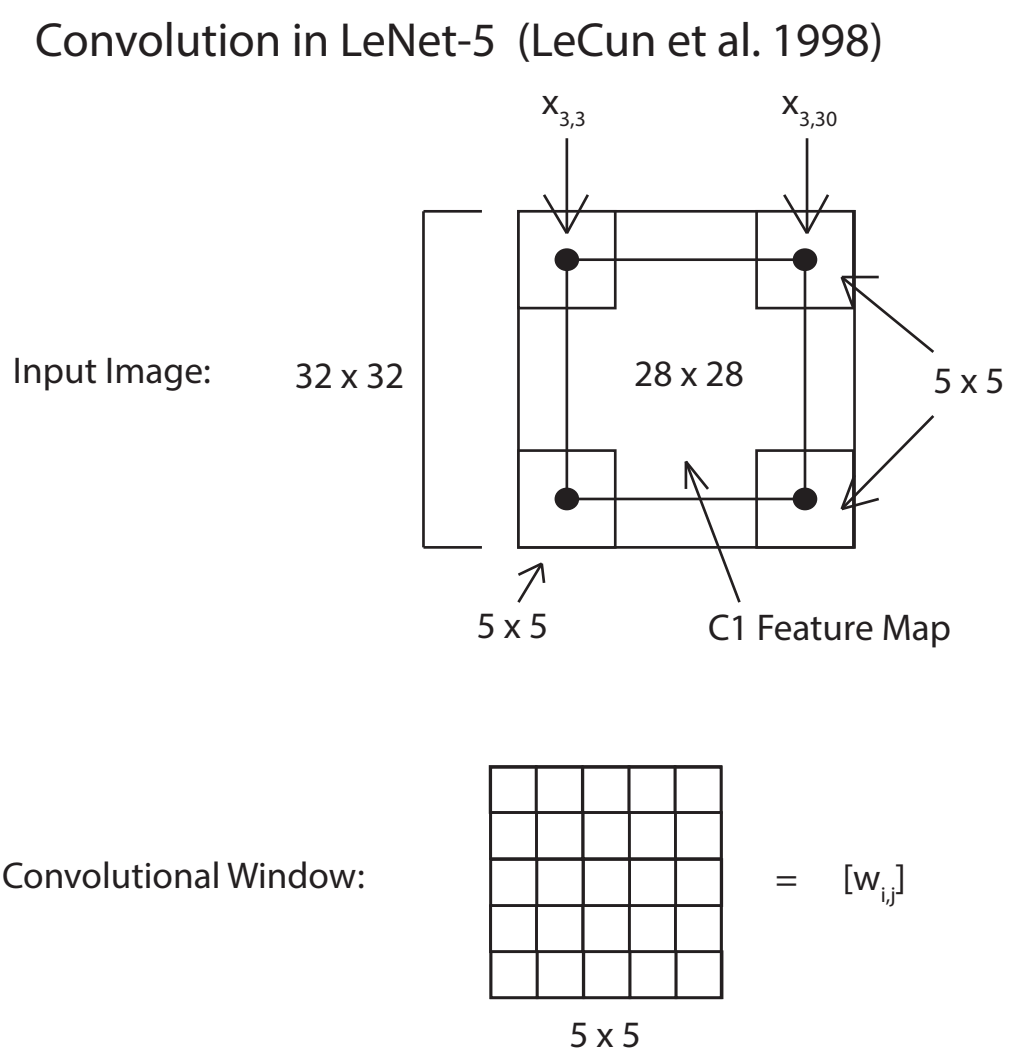

Figure 3.2: Details of the convolutional operator used by LeNet-5 CNN.

$$= [w_{i,j}] = \begin{bmatrix} w_{-2,-2} & w_{-2,-1} & w_{-2,0} & w_{-2,1} & w_{-2,2} \\ w_{-1,-2} & w_{-1,-1} & w_{-1,0} & w_{-1,1} & w_{-1,2} \\ w_{0,-2} & w_{0,-1} & w_{0,0} & w_{0,1} & w_{0,2} \\ w_{1,-2} & w_{1,-1} & w_{1,0} & w_{1,1} & w_{1,2} \\ w_{2,-2} & w_{2,-1} & w_{2,0} & w_{2,1} & w_{2,2} \end{bmatrix} \tag{3.4}$$

where $i = -2, 2$ and $j = -2, 2$.

Let $y_{i,j}$ be pixel values in any feature map of C1.

$$y_{i,j} = \sum_{k=-2}^{2} \sum_{l=-2}^{2} w_{k,l} x_{i-k,-j-l} \text{ - convolution, i = 3,...,30, j = 3,...,30} \tag{3.5}$$

$$y_{i,j} = \sum_{k=-2}^{2} \sum_{l=-2}^{2} w_{k,l} x_{i+k,j+l} \text{ - correlation} \tag{3.6}$$

where, $x_{i,j}$ are pixels in the image, $i = 1, ..., 32$ and $j = 1, ..., 32$

In the case of the LeNet-5 example shown in Figure 3.1, this particular network has a 32x32 input layer, which is convolved, as described in Figure 3.2, in the first convolutional layer (C1) using a 5x5 receptive field to produce 6 feature maps of size 28x28 each. This produces 150 weights plus 6 biases to create 156 free parameters and a grand total of 117,600 weights + 4,704 biases = 122,304 connections.

The next layer is the first subsampling layer (S2), and this applies a 2x2 receptive field to produce 6 feature maps of size 14x14 each. This layer has 6 weights plus 6 biases for a total of 12 free parameters and a grand total of 4,704 weights + 1,176 biases = 5,880 connections.

The next layer is the second convolutional layer (C3). It convolves the previous layer's output using a 5x5 receptive field to produce 16 feature maps of size 10x10 each. It implements a special sparse connection scheme such that the first six feature maps are connected to three contiguous feature maps from the previous layer, the next six feature maps are connected to four contiguous feature maps from the previous layer, the next three feature maps are connected to four non-contiguous feature maps from the previous layer, and the last feature map is connected to every feature map from the previous layer. Thus, there are 60 sets of connections, instead of 96 as would be expected if the connections were complete. This produces 1,500 weights plus 16 biases to create 1,516 free parameters and a

grand total of 150,000 weights + 1600 biases = 151,600 connections.

The next layer is the second subsampling layer (S4), and this applies a 2x2 receptive field to produce 16 feature maps of size 5x5 each. This layer has 16 weights plus 16 biases for a total of 32 free parameters and a grand total of 1,600 weights + 400 biases = 2,000 connections.

Next in line we have the third and final convolutional layer (C5). It convolves the previous layer's output using a 5x5 receptive field to produce 120 feature maps of size 1x1 each. This produces 48,000 weights plus 120 biases to create 48,120 free parameters and connections.

The next layer is a fully connected layer (F6) containing 84 nodes, which brings about 10,080 weights plus 84 biases to create 10,164 connections.

The final output layer of the original LeNet-5 was actually an Radial Basis Function layer that had each node compute the Euclidian Radial Basis Function for each class. This layer has 840 connections to the previous layer.

This brings the total number free parameters in the network to 60,840 and the total number of connections in the network to 340,908.

As can be seen from the LeNet-5 example, the apparent complexity of the CNN comes mostly from its unique structural properties, which introduce a number of hyper-parameters, such as feature map numbers, and receptive field sizes.

3.3 Theoretical Analysis

CNNs have particularly many hyper-parameters due to the structure of the network. Determining the optimal hyper-parameters can appear to be a bit of an art. In particular, the number of feature maps for a given convolutional layer tends to be chosen based on empirical performance rather than on any sort of theoretical justification [51]. Numbers in the first convolutional layer range from very small (3-6) [29], [39], to very large (96-1600) [10], [11], [16], [28].

One wonders then, if there is some sort of theoretical rationale that can be used to determine the optimal number of feature maps, given other hyper-parameters. In particular, one would expect that the dimensions of the receptive field, ought to have some influence on this optimum [8].

A receptive field of width r consists of r^2 elements or nodes. If we have feature maps m then, the maximum number of possible feature maps before duplication, given an 8-bit grey scale image is 256^{r^2}. Since the difference between a grey level of say, 100 and 101, is roughly negligible, we simplify and reduce the number of bins in the histogram so to speak from 256 to 2. Looking at binary features as a way of simplifying the problem is not unheard of [5]. So, given a binary image the number of possible binary feature maps before duplication is

$$\Omega = 2^{r^2}, \tag{3.7}$$

which is still a rapidly increasing number.

Let's look at some very simple receptive fields. Take a receptive field of size 1x1. How many feature maps would it take before additional maps become completely redundant? Applying Ω would suggest two.

Now take a receptive field of size 2x2. How many feature maps would it take before additional maps become completely redundant? Applying Ω would suggest 16. What about 3x3? 512. What about 4x4? 65536. These values represent an upper bound, beyond which additional feature maps should not improve performance significantly. But clearly, not even all of these feature maps would be all that useful. If we look again at a 2x2 receptive field, regarding those 16 non-redundant feature maps, shown in Figure 3.3, are all of them necessary? Assuming that we have a higher layer that combines features, many of these are actually redundant in practice, or don't encode anything useful.

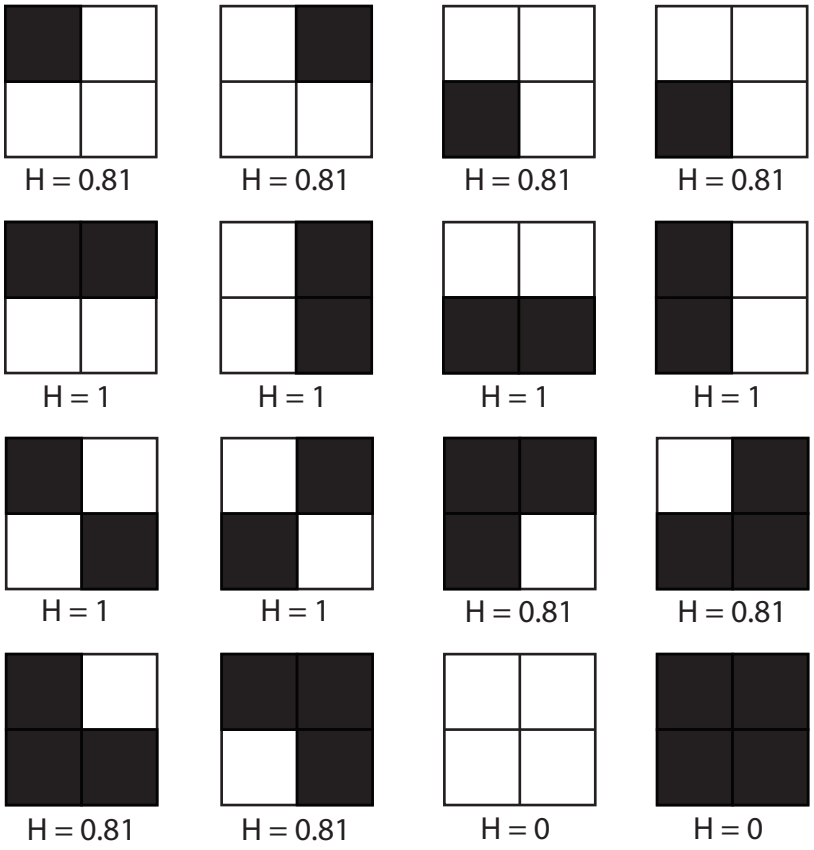

Figure 3.3: The 16 possible binary feature maps of a 2x2 receptive field, with their respective entropy values.

So how do we determine which ones are useful? Borrowing from Information Theory, we can look at how much information each map encodes. Consider Shannon entropy or the

amount of information given

$$H(X) = -\sum_{i=1}^{n} p(x_i) \log_2 p(x_i). \tag{3.8}$$

Thus, we calculate the Shannon entropy of each feature map, again, shown in Figure 3.3. The combined set has an average Shannon entropy of 0.7806. What's interesting here is that we can group the Shannon entropy values together. In the 2x2 case, there are six patterns equal to an entropy of 1, while there are eight patterns with an entropy of around 0.81, and two patterns with an entropy of 0. Thus we have three bins of entropy values so to speak.

Thus, we hypothesize a very simple theoretical method, one that admittedly simplifies a very complex problem. Shannon entropy has the obvious disadvantage that it does not tell us about the spatial relationship between neighbouring pixels. And again, we assume binary feature maps. Nevertheless, we propose this as an initial attempt to approximate the underlying reality.

The number of different possible entropy values for the total binary feature map set of a particular receptive field size is determined by considering the number of elements in a receptive field r^2. The number of unique ways you can fill the binary histogram of the possible feature maps then is $r^2 + 1$. But roughly half the patterns are inverses of each other. So the actual number of unique entropy values is $(r^2+1)/2$ if r is odd. Or $(r^2)/2+1$ if r is even.

Given the the number of different entropy values

$$h(r) = \begin{cases} \frac{r^2+1}{2} & \text{if } r \text{ is odd} \\ \frac{r^2}{2} + 1 & \text{if } r \text{ is even} \end{cases} \tag{3.9}$$

the number of useful feature maps is

$$u = h + s, \tag{3.10}$$

where s is a term that describes the additional useful feature maps above this minimum of h. We know from the 1x1 receptive field feature map set that s is at least 1, because when $r = 1$, the receptive field is a single pixel filter, and optimally functions as a binary filter. In such a case, $u = \Omega = 2$. In the minimum case that $s = 1$, then in the case of 1x1, $u = 2$. In the case of 2x2, $u = 4$. In the case of 3x3, $u = 6$. This is a lower bound on u that we shall use until we can determine what s actually is.

To understand this, think of a receptive field that takes up the entire space of the image. If the image is 100x100, then the receptive field is 100x100. In such an instance, each feature map is essentially a template, and the network performs what is essentially template matching. Thus the number of useful feature maps is based strictly on the number of useful templates. If you have enough templates, you can approximate the data set. Any more than that would be unnecessary. To determine how many such templates would be useful, consider again, the number of different Shannon entropies in the feature set. While it is not guaranteed that two templates with the same entropy would be identical, two templates with different entropies are certainly different. Also consider the difference between that 100x100 receptive field, and a 99x99 receptive field. The differences between the two in terms of number of useful feature maps intuitively seems negligible. This suggests that s is either a constant, or at most a linearly increasing term. One thing else to consider is that as h increases, the distance between various entropies decreases, to the point where many of the values start to become nearly the same. Thus, one will expect that for very high values of r, u will be too high.

Some possibilities for s that we propose to consider are based on the notion of the way in which square lattices can be divided into different types of squares based on their

position. For 1x1, there is only one square with no adjacent squares, but for 2x2 there are exactly four corner squares. A 3x3 receptive field also has exactly four corner squares, but also four edge squares and one inner square. A 4x4 receptive field has four corner squares, eight non-corner edge squares, and four inner squares. From this we see that the number of each type of square for $r > 1$ is the constant 4 for corners, $4(r-2)$ for non-corner edge squares, and $(r-2)^2$ for inner squares. A receptive field of size 3x3 or greater has four corner regions, four edge regions, and one inner area. Thus, if we assume that positional/spatial information is relevant, then s could be at least the number of types of squares in the receptive field. This suggests that $s = 1$ for $r = 1$ and $r = 2$, and $s = 3$ for $r > 2$. Alternatively, we can assume that it is the number of distinct regions that determines s, in which case, $s = 1$ for $r = 1$, $s = 4$ for $r = 2$, and $s = 9$ for $r > 2$.

Any less than u and the theory predicts a drop in performance. Above this number the theory is agnostic about one of three possible directions. Either the additional feature maps won't affect the predictive power of the model, so we should see a plateau, or the Curse of Dimensionality will cause the predictive power of the model to begin to drop, or as seen in previous papers such as [11], the predictive power of the model will begin to increase, albeit at a slower rate.

Thus far we have taken care of the first convolutional layer. For the second convolutional layer and beyond, the question arises of whether or not to stick to this formula for u, or whether it makes more sense to increase the number of feature maps in some proportion to the number in the previous convolutional layer. Upper convolutional layers are not simply taking the pixel intensities, but instead, combining the feature maps of the lower layer. In which case, it makes sense to change the formula for u for upper layers to:

$$u_l = v u_{l-1}, \tag{3.11}$$

where v is some multiplier value and l is the layer. Candidates for this value range from

u_{l-1} itself, to some constant such as 2 or 4.

There is no substitute for empirical evidence, so we test the theory by running experiments to exhaustively search for the hypothetical, optimal number of feature maps.

3.4 Methodology

To speed up and simplify the experiments, we devised, using the Caltech-101 dataset [17], a specialized dataset, which we shall refer to as the Caltech-20. The Caltech-20 consists of 20 object categories with 50 images per category total, divided into a training set of 40 images per category, and a test set of 10 images per category. The 20 categories were selected by finding the 20 image categories with the most square average dimensions that also had at least 50 example images. The images were also resized to 100 x 100 pixels, with margins created by irregular image dimensions zero-padded (essentially blacked out). To simplify the task so as to have one channel rather than three, the images were also converted to greyscale. The training set totalled 800 images while the test set consisted of 200 images. Some example images are shown in figure 3.4.

Figure 3.4: Images from the Caltech-20 data set.

CNNs tend to require a fairly significant amount of time to train. One way to improve temporal performance is to implement these ANNs such that they are able to use the Graphical Processing Unit (GPU) of certain video cards rather than merely the CPU of a given machine [54], [55], [49], [28]. NVIDIA video cards in particular have a parallel computing platform called Compute Unified Device Architecture (CUDA) that can take full advantage of the many cores on a typical video card to greatly accelerate parallel

computing tasks. ANNs are quite parallel in nature, and thus quite amenable to this. Thus, for our implementation of the CNN, we turned to the Python-based Theano library (`http://deeplearning.net/software/theano/`) [4]. We were able to find appropriate Deep Learning Python scripts for the CNN. Our tests suggest that the speed of the CNN using the GPU improved by a factor of eight, as compared to just using the CPU.

CNNs require special consideration when implementing their architecture. A method was devised to calculate a usable set of architecture parameters. The relationship between layers can be described as follows. To calculate the reasonable dimensions of a square layer from either its previous layer (or next layer) in the hierarchy requires at least some of the following variables to be assigned. Let x be the width of the previous (or current) square layer. Let y be the width of the current (or next) square layer. Let r be the width of the square receptive field of nodes in the previous (or current) layer to each current (or next) layer node, and f be the offset distance between the receptive fields of adjacent nodes in the current (or next) layer. The relationship between these variables is best described by the equation below.

$$y = \frac{x - (r - f)}{f}, \tag{3.12}$$

where, $x \geq y$, $x \geq r \geq f$, and $f > 0$.

For convolutional layers this generalizes because f = 1, to:

$$y = x - r + 1. \tag{3.13}$$

For subsampling layers, this generalizes because r = f, to:

$$y = \frac{x}{f}. \tag{3.14}$$

From this we can determine the dimensions of each layer. To describe a CNN, we adopt a similar convention to [10]. An example architecture for the CNN on the NORB dataset [30] can be written out as:

$96 \times 96 \rightarrow 8C5 \rightarrow S4 \rightarrow 24C6 \rightarrow S3 \rightarrow 24C6 \rightarrow 100N \rightarrow 5N$, where the number before C is the number of feature maps in a convolutional layer, the number after C is the receptive field width in a convolutional layer, the number after S is the receptive field width of a subsampling layer, and the number before N is the number of nodes in a fully connected layer.

For us to effectively test a single convolutional layer, we use a series of architectures, where v is a variable number of feature maps:

$100 \times 100 \rightarrow vC1 \rightarrow S2 \rightarrow 500N \rightarrow 20N$

$100 \times 100 \rightarrow vC2 \rightarrow S3 \rightarrow 500N \rightarrow 20N$

$100 \times 100 \rightarrow vC3 \rightarrow S2 \rightarrow 500N \rightarrow 20N$

$100 \times 100 \rightarrow vC5 \rightarrow S3 \rightarrow 500N \rightarrow 20N$

$100 \times 100 \rightarrow vC99 \rightarrow S1 \rightarrow 500N \rightarrow 20N$

The reason why we sometimes use 3x3 subsampling receptive fields is that the size of the convolved feature maps are divisible by 3 but not 2. Otherwise we choose to use 2x2 subsampling receptive fields where possible. We find that, with the exception of the unique

99x99 receptive field, not using subsampling produces too many features and parameters and causes the network to have difficulty learning. The method of subsampling we use is max-pooling, which involves taking the maximum value seen in the receptive field of the subsampling layer.

For testing multiple convolutional layers, we use the following architecture, where v_i is a variable number of feature maps for each layer:

$100 \times 100 \rightarrow v_1C2 \rightarrow S3 \rightarrow v_2C2 \rightarrow S2 \rightarrow v_3C2 \rightarrow S3 \rightarrow v_4C2 \rightarrow S2 \rightarrow v_5C2 \rightarrow S1 \rightarrow 500N \rightarrow 20N$

All our networks use the same basic classifier, which is a multi-layer Perceptron with 500 hidden nodes and 20 output nodes. Various other parameters for the CNN were also experimented with to determine the optimal parameters to use in our experiments. We eventually settled on 100 epochs of training. The CNN learning rate and learning rate decrement parameters were determined by trial and error. The learning rate was initially set to 0.1, and gradually decremented to approximately 0.001.

3.5 Analysis and Results

The following figures are intentionally fitted with a trend line that attempts to test the hypothesis that a cubic function approximates the data. It should not be construed to suggest that this is in fact the underlying function.

Figure 3.5 shows the results of experimenting with different numbers of feature maps on the accuracy of the CNN trained on the Caltech-20, and using a 1x1 receptive field.

As can be seen, the accuracy quickly increases between 1 and 2 feature maps, and then levels off for more than 2 feature maps. This is consistent with the theory, albeit, the

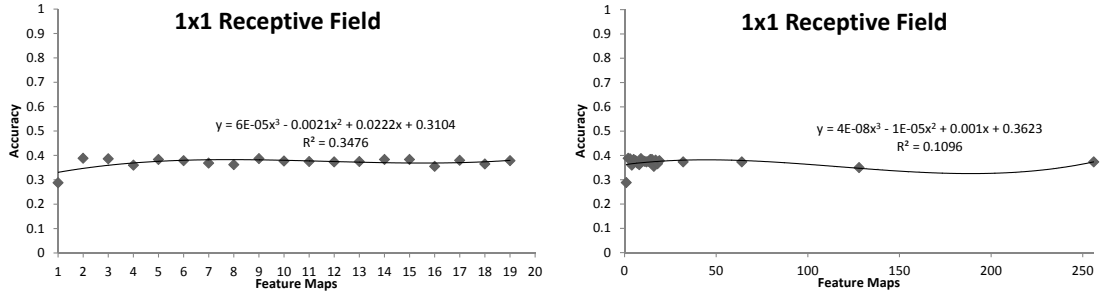

Figure 3.5: Graphs of the accuracy given a variable number of feature maps for a 1x1 receptive field.

plateau beyond seems to be neither increasing nor decreasing, which suggests some kind of saturation point around 2.

Figure 3.6 shows the results of experimenting with different numbers of feature maps on the accuracy of the CNN trained on the Caltech-20, and using a 2x2 receptive field.

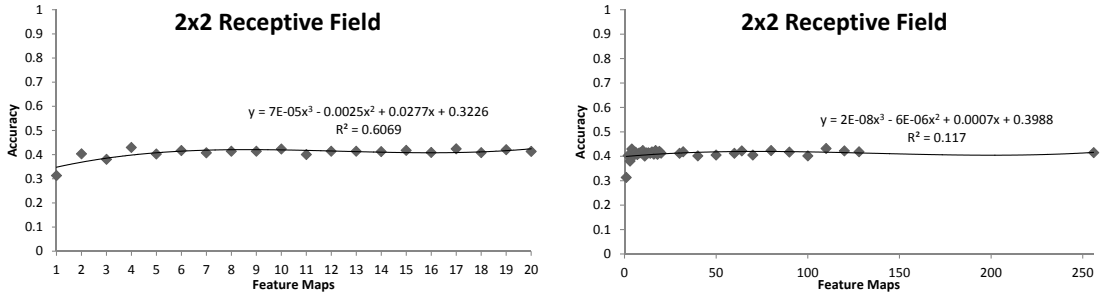

Figure 3.6: Graphs of the accuracy given a variable number of feature maps for a 2x2 receptive field.

As can be seen, the accuracy quickly increases between 1 and 4 feature maps, and then levels off for more than 4 feature maps. This is consistent with the theory where $s = 1$. The plateau beyond seems to be neither increasing nor decreasing, which suggests some kind of saturation point around 4.

Figure 3.7 shows the results of experimenting with different numbers of feature maps on the accuracy of the CNN trained on the Caltech-20, and using a 3x3 receptive field.

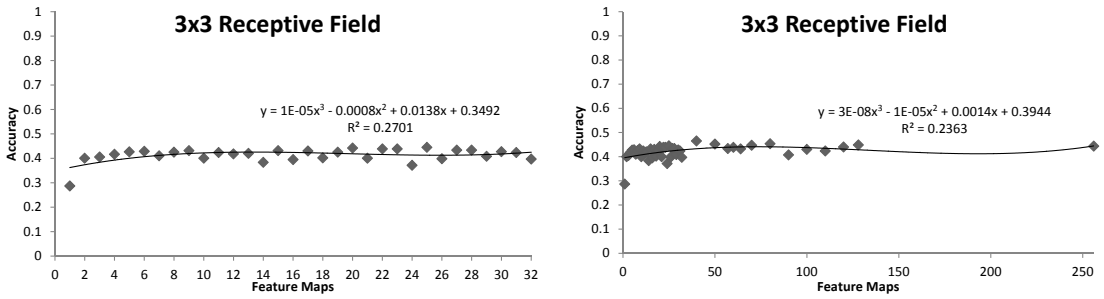

Figure 3.7: Graphs of the accuracy given a variable number of feature maps for a 3x3 receptive field.

As can be seen, the accuracy increases between 1 and 6 feature maps, and then proceeds to plateau somewhat erratically. Unlike the previous receptive field sizes however, there are accuracies greater than that found at u. The plateau also appears less stable. Predicted u values of 8 and 14 don't appear to correlate well.

Figure 3.8 shows the results of experimenting with different numbers of feature maps on the accuracy of the CNN trained on the Caltech-20, and using a 5x5 receptive field.

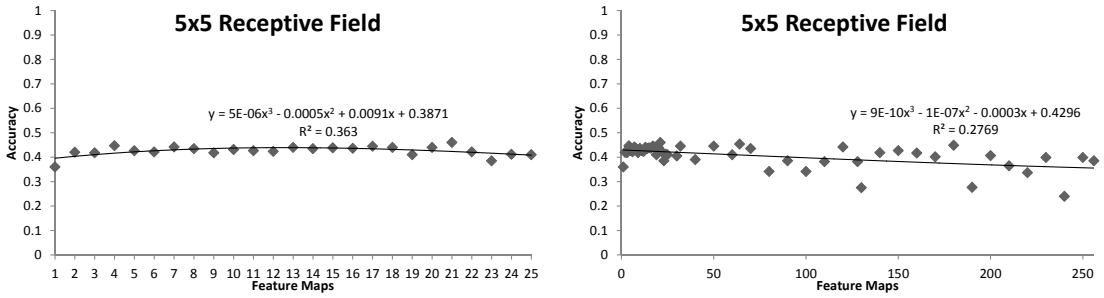

Figure 3.8: Graphs of the accuracy given a variable number of feature maps for a 5x5 receptive field.

As can be seen, the accuracy quickly increases between 1 and 4 feature maps, and then plateaus for a while before spreading out rather chaotically. This may be explained by some combination of overfitting, the curse of dimensionality, or too high a learning rate causing failure to converge. At 21 there is a high point of 46% which is close to our predicted

u value of 22, if $s = 9$.

Figure 3.9 show the results of experimenting with different numbers of feature maps on the accuracy of the CNN trained on the Caltech-20, and using a 99x99 receptive field.

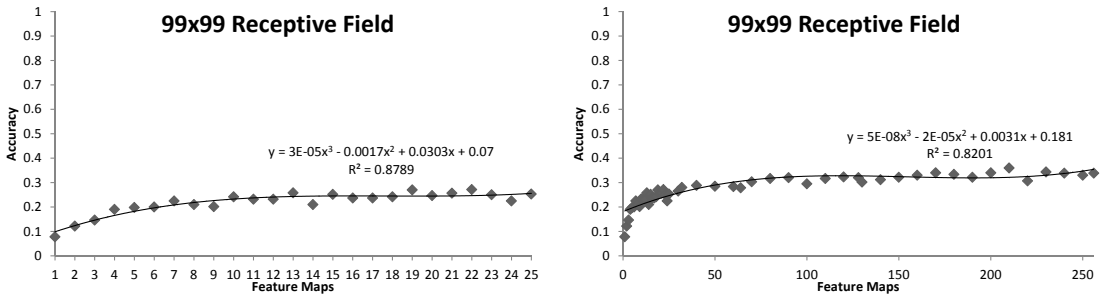

Figure 3.9: Graphs of the accuracy given a variable number of feature maps for a 99x99 receptive field.

As can be seen, the accuracy steadily increases between 1 and 210 feature maps, and then begins to plateau. As predicted, our u value of 4901 is much too high for the very large value of $r = 99$.

Lastly, we look at the effect of multiple convolutional layers. Figure 3.10 shows what happens when the first layer of a 12 layer CNN with 5 convolutional layers is held constant at 4 feature maps, and the upper layers are multiplied by the number in the layer before it. So for a multiple v of 2, the feature maps for each layer would be 4, 8, 16, 32, 64, respectively. We refer to this as the pyramidal structure.

Clearly, increasing the number of feature maps in the upper layers has a significant impact. Perhaps not coincidentally, the best performing architecture we have encountered so far was this architecture with 4, 20, 100, 500, and 2500 feature maps in each respective layer. It achieved an accuracy of 54.5% on our Caltech-20 data set. This can be contrasted with the effect of having the same number of feature maps in each layer as shown in figure 3.11. We refer to this as the equal structure.

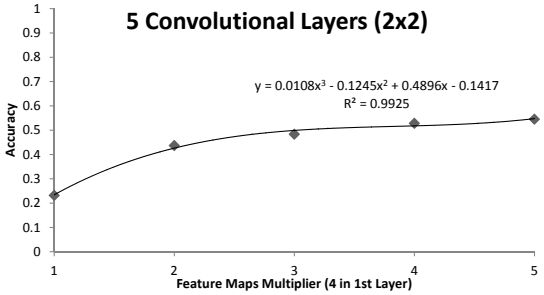

Figure 3.10: Graph of the accuracy given a variable number of feature maps for a network with 5 convolutional layers of 2x2 receptive field. Here the higher layers are a multiple of the lower layers.

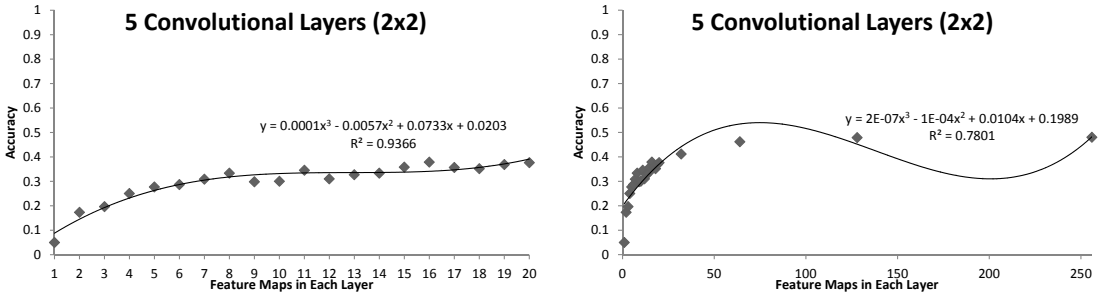

Figure 3.11: Graph of the accuracy given a variable number of feature maps for a network with 5 convolutional layers of 2x2 receptive field. Here each layer has the same number of feature maps.

While the accuracy rises with the number of feature maps as well, it should be noted that for the computational cost, the pyramidal structure appears to be a better use of resources than the equal structure.

3.6 Discussion

It appears that the theoretical method seems to hold well for receptive fields of size 1x1, and 2x2. For larger sizes, the data is not as clear. The data from the 3x3 and 5x5 receptive field experiments suggests that there can be complicating factors involved that cause the

data to spread. Such factors could include, the curse of dimensionality, and also, technical issues such as failure to converge due to too high a learning rate, or overfitting. As our experimental set up is intentionally very simple, we lack many of the normalizing methods that might otherwise improve performance. The data from the 99x99 receptive field experiment is interesting because it starts to plateau much sooner than predicted by the equation for u. However, we mentioned before that this would probably happen with the current version of u. The number of different entropies at $r = 99$ are probably very close together and an improved u equation should take this into account.

It should also be emphasized that our results could be particular to our choice of hyper-parameters such as learning rate and our choice of a very small dataset.

Nevertheless, what we do not find, is the clear and simple monotonically increasing function seen in [11], and [16]. Rather, the data shows that after an initial rise, the function seems to plateau and it is uncertain whether it can be construed to be rising or falling or stable. Even in the case of the 99x99 receptive field, past 210 feature maps, we see what appears to be the beginnings of such a plateau.

This is not the case with highly layered networks however, which do appear to show a monotonically increasing function in terms of increasing the number of feature maps. However, this could well be due to the optimal number of feature maps in the last layer being exceedingly high due to multiplier effects.

One thing that could considerably improve our work would be finding some kind of measure of spatial entropy rather than relying on Shannon entropy. The problem with Shannon entropy is of course, that it does not consider the potential information that comes from the arrangement of neighbouring pixels. We might very well improve our estimates of u by taking into consideration the spatial entropy in h, rather than relying on the s term.

Future work should likely include looking at what the optimal receptive field size is.

Our experiments hint at this value as being greater than 3x3 and [11] suggests that it is less than 8x8, but performing the exhaustive search without knowing the optimal number of feature maps for each receptive field size is a computationally complex task.

As with [28], we find that more convolutional layers seems to improve performance. The optimal number of such layers is something else that should be looked at in the future.

3.7 Conclusions

Our experiments provided some additional data to consider for anyone interested in optimizing a CNN. Though the theoretical method is not clear beyond certain extremely small or extremely large receptive fields, it does suggest that there is some relationship between the receptive field size and the number of useful feature maps in a given convolutional layer of a CNN. It nevertheless may prove to be a useful approximation.

Our experiments also suggest that when comparing architectures with equal numbers of feature maps in each layer with architectures that have pyramidal schemes where the number of feature maps increase by some multiple, that the pyramidal methods use computing resources more effectively.

In any case, we were unable to determine clearly the optimal number of feature maps for receptive fields larger than 2x2. Thus, for subsequent experiments, we rely on the feature map numbers that are used by papers in the literature to determine our architectures.

Chapter 4

Deep Belief Networks

One of the more recent developments in machine learning research has been the Deep Belief Network (DBN). The DBN is a recurrent ANN with undirected connections. Structurally, it is made up of multiple layers of RBMs, such that it can be seen as a 'deep' architecture. To understand how this is an effective structure, we must first understand the basic nature of a recurrent ANN.

Recurrent ANNs differ from feed-forward ANNs in that their connections can form cycles. Such networks cannot use simple Backpropagation or other feed-forward based learning algorithms. The advantage of recurrent ANNs is that they can possess associative memory-like behaviour. Early Recurrent ANNs, such as the Hopfield network [25], showed promise in this regard, but were limited. The Hopfield network was only a single layer architecture that could only learn very limited problems due to limited memory capacity. A multi-layer generalization of the Hopfield Network was developed known as the Boltzmann Machine [1], which while able to store considerably more memory, suffered from being overly slow to train.

A Boltzmann Machine is an energy-based model [3] [22]. This represents an analogy

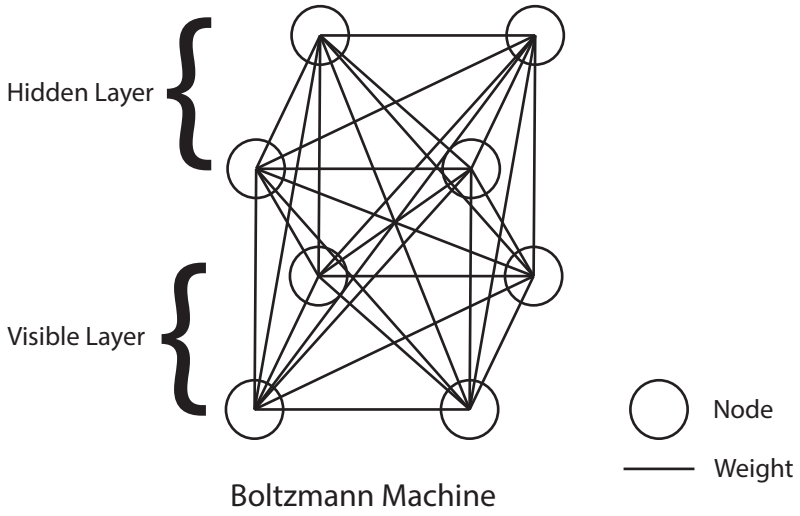

Figure 4.1: The structure of the general Boltzmann Machine.

from physics, and in particular, statistical mechanics [15]. It thus has a scalar energy that represents a particular configuration of variables. A physical analogy of this would be to imagine that the network is representative of a number of physical magnets, each of which can be either positive or negative (+1 or -1). The weights are functions of the physical separations between the magnets, and each pair of magnets has an associated interaction energy that depends on their state, separation, and other physical properties. The energy of the full system is thus the sum of these interaction energies.

Such an energy-based model learns by changing its energy function such that it has a shape that possesses desirable properties. Commonly, this corresponds to having a low or lowest energy, which is the most stable configuration. Thus we try to find a way to minimize the energy of a Boltzmann Machine. The energy of a Boltzmann Machine can be defined by:

$$E(x,h) = \sum_{i \in visible} a_i x_i - \sum_{j \in hidden} b_j h_j - \sum_{i,j} x_i h_j w_{i,j} - \sum_{i,j} x_i x_j u_{i,j} - \sum_{i,j} h_i h_j v_{i,j} \qquad (4.1)$$

This in turn is applied to a probability distribution:

$$P(x) = \frac{e^{-E(x)}}{Z} \tag{4.2}$$

where Z is the partition function:

$$Z = \sum_{x} e^{-E(x)} \tag{4.3}$$

We modify these equations to incorporate hidden variables:

$$P(x,h) = \frac{e^{-E(x,h)}}{Z} \tag{4.4}$$

$$P(x) = \sum_{h} P(x,h) = \sum_{h} \frac{e^{-E(x,h)}}{Z} \tag{4.5}$$

$$Z = \sum_{x,h} e^{-E(x,h)} \tag{4.6}$$

The concept of Free Energy is borrowed from physics, where it is the useable subset of energy, also known as the available energy to do work after subtracting the entropy, and represents a marginalization of the energy in the log domain:

$$F(x) = -\log \sum_{h} e^{-E(x,h)} \tag{4.7}$$

and

$$Z = \sum_{x} e^{-F(x)} \tag{4.8}$$

Next we derive the data log-likelihood gradient.

Let's rewrite Equation (4.5) using Free Energy as follows:

$$\begin{aligned} P(x) &= \frac{1}{Z} \sum_{h} e^{-E(x,h)} \\ &= \frac{1}{Z} e^{-[-\log \sum_{h} e^{-E(x,h)}]} \\ &= \frac{1}{Z} e^{-F(x)} \end{aligned} \tag{4.9}$$

Let θ represent the parameters (the weights) of the model. The data log-likelihood gradient thus becomes:

$$\begin{aligned} \frac{\partial \log P(x)}{\partial \theta} &= \frac{\partial}{\partial \theta} \left(\log \frac{e^{-F(x)}}{Z} \right) \\ &= \frac{\partial}{\partial \theta} \left[\log e^{-F(x)} - \log Z \right] \\ &= \frac{\partial}{\partial \theta} \left[-F(x) - \log Z \right] \\ &= -\frac{\partial F(x)}{\partial \theta} - \frac{1}{Z} \frac{\partial Z}{\partial \theta} \end{aligned} \tag{4.10}$$

Using the definition of Z given in Equation (4.8), and shown in Equation (4.9) and Equation (4.10), we have:

$$\begin{aligned}\frac{\partial \log P(x)}{\partial \theta} &= -\frac{\partial F(x)}{\partial \theta} - \frac{1}{Z}\sum_{x}\frac{\partial}{\partial \theta}e^{-F(x)} \\ &= -\frac{\partial F(x)}{\partial \theta} + \frac{1}{Z}\sum_{x} e^{-F(x)} \cdot \frac{\partial F(x)}{\partial \theta} \\ &= -\frac{\partial F(x)}{\partial \theta} + \sum_{x} P(x)\frac{\partial F(x)}{\partial \theta} \end{aligned} \tag{4.11}$$

Having this gradient allows us to perform stochastic gradient descent as a way of finding that desired lowest energy state mentioned earlier. However, in practice, this gradient is difficult to calculate for a regular Boltzmann Machine, and while not intractable, it is a very slow computation.

A variant of the Boltzmann Machine was first known as a Harmonium [52], but later called a RBM, which initially saw little use. Then Hinton [21] developed a fast learning algorithm for RBMs called Contrastive Divergence, which uses Gibbs sampling within a gradient descent process. The RBM is primarily different from a regular Boltzmann Machine by the simple fact that it lacks the lateral or sideways connections within layers. As such, an RBM can be defined by the simpler energy function as follows:

$$E(v,h) = \sum_{i \in visible} a_i v_i - \sum_{j \in hidden} b_j h_j - \sum_{i,j} v_i h_j w_{i,j} \tag{4.12}$$

where v_i and h_j are the binary states of the visible unit i and hidden unit j, a_i and b_j are their biases, and $w_{i,j}$ is the weight connection between them [22].

Applying the data log-likelihood gradient from earlier, we can now find the derivative

of the log probability of a training vector with respect to a weight:

$$\frac{\partial \log p(v)}{\partial w_{ij}} = \langle v_i h_j \rangle_{data} - \langle v_i h_j \rangle_{model} \tag{4.13}$$

where, the angle brackets enclose the expectations of the distribution labeled in the subscript. And thus, the change in a weight in an RBM is given by the learning rule:

$$\Delta w_{i,j} = \epsilon(\langle v_i h_j \rangle_{data} - \langle v_i h_j \rangle_{model}) \tag{4.14}$$

where ϵ is the learning rate.

$\langle v_i h_j \rangle_{data}$ is fairly easy to calculate. If you take a randomly selected training vector v, then the binary state h_j of each of the hidden units is 1 with probability:

$$p(h_j = 1|v) = \sigma(b_j + \sum_i v_i w_{ij}) \tag{4.15}$$

where $\sigma(x)$ a logistic sigmoid function such as $1/(1 + exp(-x))$.

Similarly, given a hidden vector h_j with weights w_{ij}, we can get an unbiased sample of the state of a visible unit:

$$p(v_i = 1|h) = \sigma(a_i + \sum_j h_j w_{ij}) \tag{4.16}$$

$\langle v_i h_j \rangle_{model}$ is much more difficult to calculate, and so we use an approximation $\langle v_i h_j \rangle_{recon}$ instead. Basically this reconstruction consists of first setting the visible units to a training vector, then computing the binary states of the hidden units in parallel with equation 4.15. Next, set each v_i to 1 with a probability according to equation 4.16, and we

get a reconstruction.

$$\Delta w_{i,j} = \epsilon(\langle v_i h_j \rangle_{data} - \langle v_i h_j \rangle_{recon}) \tag{4.17}$$

This learning rule attempts to approximate the gradient of an objective function called the Contrastive Divergence (which itself is an approximation of the log-likelihood gradient), though it is not actually following the gradient. Despite this, it works quite well for many applications, and is much faster than the previously mentioned way of learning regular Boltzmann Machines.

By stacking RBMs together, Hinton, Osindero, & Teh, [23] created the DBN. The DBN is trained in a greedy, layer-wise fashion. This generally involves pre-training each RBM separately starting at the bottom layer and working up to the top layer. All layers have their weights initialized using unsupervised learning in the pre-training phase, after which fine-tuning using Backpropagation is performed using the labeled data, training in a supervised manner.

Mathematically, we can describe a DBN with l layers according to the joint distribution below, given an observed vector x, and l hidden layers h^k [3].

$$P(x, h^1, ..., h^l) = \left(\prod_{k=0}^{l-2} P(h^k | h^{k+1}) \right) P(h^{l-1}, h^l) \tag{4.18}$$

In this case, $x = h^0$, while $P(h^{k-1}|h^k)$ is a visible-given-hidden conditional distribution in the RBM at level k of the DBN, and $P(h^{l-1}, h^l)$ is the top-level RBM's joint distribution.

When introduced, the DBN produced then state of the art performance on such tasks

as the MNIST. Later DBNs were also applied to 3D object recognition [37]. Ranzato, Susskind, Mnih, & Hinton [44] also showed how effective DBNs could be on occluded facial images.

Chapter 5

Methodology

In order to contrast the effectiveness of the DBNs generative model with discriminative models, we compared several models of ANN, as well as other machine learning algorithms, including: SVM, CNN, (two discriminative models) and DBN, (one generative model). Although the SVM is not a normal ANN strictly speaking, its popularity as a discriminative classifier means that it deserves inclusion as a control.

Two object/image datasets were used, the Caltech-101 [17], and the small NORB [30]. These were chosen for their popularity in the literature. The Caltech-101 consists of 101 object categories and at least 31 images per category. The small NORB consists of 5 object categories and several thousand images per category, for a total of 24300 images each in the training and test sets. The small NORB proper includes a pair of stereo images for each training example, but we chose to only use one of the images in the pair.

To conduct test runs and identify the best parameters, a simpler problem was devised using the Caltech-101 dataset, which we shall refer to as the Caltech-20. This consisted of taking 20 object categories with 50 images per category. The 20 categories were selected by finding the 20 image categories with the most square average dimensions that also had

at least 50 example images. The images were also resized to 100 x 100 pixels, with margins created by irregular image dimensions zero-padded (essentially blacked out). To simplify the task so as to have one channel rather than three, the images were also converted to greyscale. The training set totalled 800 non-occluded images and 800 occluded images while the test set consisted of 200 non-occluded images and 200 occluded images. Non-occluded images with the object fully visible in the image are shown in figure 5.1.

Figure 5.1: Images from the Caltech-20 non-occluded test set.

Occluded images were created by occluding a random half of each image in the test set with zeroes (black) as seen in figure 5.2. For most of our early experiments we trained the classifier on just the 800 non-occluded training images, and then tested the classifier on both the 200 non-occluded test images and the 200 occluded test images. However, the option to train the classifier on both the non-occluded and occluded images was available and at times utilized.

Figure 5.2: Images from the Caltech-20 occluded test set.

Various parameters for the various learning algorithms were tested on the Caltech-20 to find the optimal settings for performance on the main dataset problems as shown in table 5.1.

For the SVMs we tested various parameters from the literature, such as Huang & LeCun [26] and Ranzato et al. [43] and eventually settled on a Gamma value of 0.0005, and a C value of 40. Gamma is how far a single training example affects things, with low values being "far" and high values being "close". C is the tradeoff between misclassifying as few

Table 5.1: Results of experiments with SVM on the Caltech-20 to determine best parameter configuration.

SVM Selection			Parameters		Accuracy on RAW Test		
Called	**Source**	**Version**	**Gamma**	**C**	**Training**	**Non-Occluded**	**Occluded**
SVM1	Default		0.0001	1	0.359	0.315	0.130
SVM2	Ranzato et al.		5.6E-07	2100	0.726	0.320	0.130
SVM3	Huang & LeCun	SVM	0.0001	40	0.966	0.370	0.185
SVM4	Huang & LeCun	SVM/CNN	0.2	1	1.000	0.080	0.070
	Huang & LeCun	SVM	0.0005	40	1.000	0.380	0.135

Note: Configurations mainly based on papers in the literature.

training samples as possible (high C) and a smooth decision surface (low C). For code for the SVMs, we used the library "LIBSVM" by Chih-Chung Chang and Chih-Jen Lin from the National Taiwan University [7].

For the CNN, Sirotenko's Matlab library "CNN Convolutional neural network class" (`http://www.mathworks.com/matlabcentral/fileexchange/24291-cnn-convolutional-neural-network-class`) was used and modified extensively to serve our purposes. Using the method and equations from Chapter 3, we can determine the dimensions of each layer for the Caltech-20 as seen in table 5.2, where S, C and F represent convolutional, subsampling and fully connected layers, respectively.

Table 5.2: The architecture of the CNN used on the Caltech-20.

Layer	**Nodes**	**k or r**	**Feature Maps**	**Connections**	
				Actual	Theoretical
S1	100x100				
C2	96x96	5	8	200	1843200
S3	24x24	4	8	8	73728
C4	20x20	5	32	6400	2560000
S5	5x5	4	32	32	12800
C6	1x1	5	128	102400	102400
F1	512	1		65536	33554432
F2	20	1		10240	204800
Total Connections:				184816	38351360

Note: Connections are raw weights excluding biases.

Similarly, the architecture for the CNN on the Caltech-101 dataset can also be engineered as shown in table 5.3.

Table 5.3: The architecture of the CNN used on the Caltech-101, based on Ranzato et al. [43].

CNN					Connections	
Layer	**Formula**	**Nodes**	**k or r**	**Feature Maps**	**Actual**	**Theoretical**
S1	140					
C2	140-9+1=132(64)	132x132	9	64	5184	90326016
S3	132/4=33(64)	33x33	4	64	64	1115136
C4	33-9+1=25(512)	25x25	9	512	2654208	1658880000
S5	25/5=5(512)	5x5	5	512	512	320000
F1	200	200	1		102400	20480000
F2	101	101	1		20200	2040200
Total Connections:					2782568	1773161352

Note: Connections are raw weights excluding biases.

And the architecture for the CNN on the NORB dataset can be determined as seen in table 5.4.

Table 5.4: The architecture of the CNN used on the NORB dataset, based on Huang & LeCun [26].

CNN				Connections	
Layer	**Nodes**	**k or r**	**Feature Maps**	**Actual**	**Theoretical**
S1	96x96				
C2	92x92	5	8	200	1692800
S3	23x23	4	8	8	67712
C4	18x18	6	24	6912	2239488
S5	6x6	3	24	24	7776
C6	1x1	6	24	20736	20736
F1	100	1		2400	240000
F2	5	1		500	2500
Total Connections:				30780	4271012

Note: Connections are raw weights excluding biases.

Various parameters for the CNN were also experimented with as shown in table 5.5. We eventually settled on 100 epochs of training.

We also ran experiments to compare the speed of the various computers being used. These can be seen in table 5.6.

For the NORB dataset, the CNN learning rate and learning rate decrement parameters

Table 5.5: Experiments conducted using the CNN algorithm and different parameters on the Caltech-20.

Parameter Testing - CNN						
Parameters			Accuracy			Time
Epochs	teta	teta_dec	Training	Non-Occluded	Occluded	Seconds
3	0.015	0.15		0.302	0.131	859.1
10	0.010	0.50		0.326	0.160	2799.5
3	0.015	0.50		0.288	0.143	834.4
20	0.010	0.80		0.328	0.180	5629.8
50	0.020	0.90		0.361	0.152	14067.9
50	0.020	0.90	0.943	0.385	0.140	14226.9
3	0.015	0.15	0.381	0.288	0.145	832.6
10	0.010	0.50	0.416	0.310	0.151	2799.4
20	0.010	0.80	0.563	0.338	0.192	5651.4
50	0.020	0.90	0.919	0.361	0.145	14146.3
100	0.040	0.90	0.983	0.330	0.118	28647.0

Note: Epochs indicates the number of times the network was trained on the training data. Teta is the learning rate variable. Teta_dec is the multiplier by which the Teta is decreased in each Epoch.

were determined by using Huang and LeCun's [26] recommendations. That is to say, the learning rate was initially set to 2.00E-05, and gradually decremented to approximately 2.00E-07.

For the DBN we used Stansbury's Matlab library "Matlab Environment for Deep Architecture Learning (MEDAL)" (`https://github.com/dustinstansbury/medal`). Experiments were also conducted on the parameters for the DBN as seen in table 5.7. By default, DBNs use binary visible units. A modification has been suggested to use Gaussian visible units for image data [24]. DBNs using both binary and Gaussian visible units were tested (see: table 5.8).

An ANN is generally divided into layers, with the first layer being the input or visible layer containing visible units, while the last layer is the output layer. In between these two layers, can be any number of hidden layers containing hidden nodes. For the purposes of experimentation, two different types of visible units, binary and Gaussian, were used, while two different amounts of hidden nodes were used as well, 2000 and 4000 respectively for the binary units. This was because prior experiments used to determine the effectiveness

Table 5.6: A comparison of various computers and Matlab versions in terms of the speed of performing a 3 Epoch CNN run on the MNIST.

Speed Testing - CNN				
Computer		Time		CPU
		Seconds	Ratio	
Rouncey	CNN on MNIST:	1590.4	1.21	
	cudaCNN on MNIST:	71.9		
	Times faster:	22.1		
	Normal Test:	72.2		
	CUDA Test:	1.7		
Palfrey	CNN on MNIST:	1309.1		
	Normal Test:	68.7		
Sylfaen	CNN on MNIST:	485.4	2.70	12%
2009b	Normal Test:	21.8		
	cudaCNN on MNIST:	34.9		14%
	CUDA Test:	0.7		
Sylfaen	CNN on MNIST:	1169.6		45%
2011a	Normal Test:	65.0		
	cudaCNN on MNIST:	34.9		
	CUDA Test:	0.7		
Destrier	CNN on MNIST:	984.5		51%
2011a	Normal Test:	53.2		
32-bit	cudaCNN on MNIST:	20.6		
	CUDA Test:	0.3		
Destrier	CNN on MNIST:	931.3	1.26	
2011a 64-bit	Normal Test:	51.0		
Panzer	CNN on MNIST:	766.2	1.22	
2011a 64-bit	Normal Test:	44.0		

Note:
Computer Rouncey has an Intel Core 2 Duo T5750 2.0 GHz processor and 4 GB of RAM.
Computer Palfrey has an Intel Core i3 M370 2.4 GHz processor and 8 GB of RAM.
Computer Sylfaen has an Intel Xeon X3450 2.67 GHz processor and 4 GB of RAM.
Computer Destrier has an Intel Core i7-2670QM 2.2 GHz processor and 16 GB of RAM.
Computer Panzer has an Intel Core i7-3770 3.4 GHz processor and 32 GB of RAM.

of various parameter configurations found that the binary units in combination with 2000 hidden nodes seemed to actually perform better than the combination of binary units and

4000 hidden nodes, which was different than expected. Gaussian units on the other hand, showed greater effectiveness at 4000 hidden nodes, than at 2000 hidden nodes, which was expected. For this reason, we tested multiple configurations as shown. The original raw data can be found in Appendix A.

For simplicity, we can refer to these configurations as B-2000 for binary visible units and 2000 hidden nodes, B-4000 for binary visible units and 4000 hidden nodes, and G-4000 for Gaussian visible units and 4000 hidden nodes.

The speed of various machines was also tested as shown in table 5.9, table 5.10, and table 5.11. These also showed that the time taken to run each network is proportional to the number of hidden units, and to a lesser extent the number of layers of the network. Also confirmed was that it appeared that two layer DBNs tended to have the best performance. The newer versions of Matlab also had a slight performance boost over the older versions.

In addition, a version of the DBN library was modified to test the effect of sparsity on the performance of the network as shown in table 5.12. The method we used to create sparsity was at the initialization of the network to randomly set some of the hidden node weight connections to zero using a randomized matrix of ones and zeroes. The results of this experiment show that added hard-wired randomized sparsity appears to actually decrease the performance of the network. As such, this version of the network was discarded and not used in further experiments.

As previously indicated, the amount of time required to run these neural network simulations is considerable. One way to improve temporal performance is to implement these neural networks such that they are able to use the GPU of certain video cards rather than merely the CPU of a given machine. Nvidia video cards in particular have a parallel computing platform called CUDA that can take full advantage of the many cores on a typical video card to greatly accelerate parallel computing tasks. ANNs are quite parallel

Table 5.7: The results of experiments done to test the parameters for various configurations of DBNs, on the Caltech-20.

Parameter Testing - DBN											
Parameters									Accuracy		
Layers	Hidden	Epochs	Anneal	Learning	weightdecay	eta	Momentum	Batch Size	Training	Non-Occluded	Occluded
2	1000	50	no	default		0.10		100		0.271	0.154
2	1000	50	no	CD						0.259	0.169
2	1000	50	no	SML						0.094	0.094
2	1000	50	yes	default						0.261	0.167
2	1000	100	no	default						0.263	0.166
2	1000	200	no	default						0.254	0.165
2	1000	50	no	default	TRUE					0.266	0.166
2	1000	50	no	default		0.20				0.261	0.181
2	1000	50	no	default		0.50				0.219	0.152
2	1000	50	no	default		0.01				0.180	0.145
2	1000	100	no	default		0.20				0.258	0.164
2	1000	100	no	default		0.05				0.268	0.174
2	1000	50	no	default		0.05				0.219	0.177
2	1000	50	no	default		0.10	0.9			0.212	0.167
2	1000	50	no	default		0.10	0.1		0.281	0.243	0.168
2	1000	50	no	default		0.10			0.315	0.259	0.177
2	1000	50	no	default		0.10		20	0.367	0.255	0.173
2	1000	50	no	default		0.10		10	0.355	0.231	0.142
2	2000	50	no	default		0.10		100	0.393	0.305	0.160
2	2000	100	no	default		0.10		100	0.409	0.310	0.180

Note: Layers indicates the number of RBMs in the DBN. Hidden indicates the number of hidden nodes per layer. Epochs indicates the number of times the network was trained on the training data. Anneal indicates whether or not Simulated Annealing was used. Learning indicates the type learning algorithm used, either Contrastive Divergence or Stochastic Maximum Likelihood (SML), with the default being Contrastive Divergence. Weightdecay indicates whether or not weight decay was used. Eta indicates the learning rate parameter. Momentum indicates the parameter for momentum. Batch Size indicates the number of samples in each batch fed to the network during learning.

Table 5.8: Further results of experiments done to test the parameters for various configurations of DBNs, on the Caltech-20.

Parameter Testing - DBN														
Parameters			Learning Rate		Epochs				Accuracy			Fine-Tuned Accuracy		
Visible	Layers	Hidden	RBM	Fine-Tune	RBM	Fine-Tune	begin Anneal	varyEta	Training	Non-Occluded	Occluded	Training	Non-Occluded	Occluded
Gaussian	2	2000	0.001	0.01	100	30	10	7		0.115			0.265	
Binary	2	2000	0.1	0.01	100	30	10	7		0.290			0.050	
Binary	2	2000	0.1	0.01	100	30	50	50		0.240			0.050	
Gaussian	2	2000	0.001	0.01	100	30	50	50		0.110			0.320	
Gaussian	2	2000	0.001	0.01	200	50	50	50		0.145			0.345	
Gaussian	2	2000	0.001	0.01	200	50	50	50	0.155	0.130	0.085	0.620	0.320	0.160
Gaussian	2	2000	0.001	0.01	200	50	50	50	0.168	0.135	0.105	0.636	0.350	0.20
Gaussian	2	4000	0.001	0.001	200	50	50	50	0.189	0.175	0.110	0.344	0.315	0.135
Gaussian	2	4000	0.001	0.001	200	200	50	50	0.211	0.200	0.130	0.050	0.050	0.050
Gaussian	2	4000	0.001	0.001	200	100	50	50	0.210	0.195	0.115	0.388	0.310	0.155
Gaussian	2	4000	0.001	0.001	200	50	50	50	0.206	0.180	0.090	0.336	0.315	0.145

Note: Visible indicates the type of visible unit used in the input layer. Learning Rate is divided between the learning rate for the DBN during initial learning, and during fine-tuning using Backpropagation. Epochs is similarly divided. BeginAnneal indicates at what Epoch Simulated Annealing is started. VaryEta indicates at what Epoch the learning rate starts to be varied. Accuracy is equal to 1 - Error.

Table 5.9: Early results of experiments done to test the speed of various configurations of DBNs, on the Caltech-20 using the old or Rouncey laptop computer.

Caltech-20: DBN				
Parameters		Accuracy		Time(s)
Layers	Units	Non-Occluded	Occluded	
1	100	0.160	0.135-0.200	91.8
2	100	0.195	0.130	91.5
3	100	0.155	0.110	
4	100	0.175	0.150	94.7
1	200	0.215	0.125	134.2
2	200	0.235	0.170	135.8
3	200	0.165	0.170	
4	200	0.190	0.165	142.8
1	500	0.190	0.140	260.2
2	500	0.245	0.165	282.9
3	500	0.245	0.150	
4	500	0.180	0.195	306.5
1	1000	0.260	0.140	469.5
2	1000	0.265	0.175	521.3
3	1000	0.155	0.155	
4	1000	0.170	0.110	628.9
1	2000	0.265	0.150	
2	2000	0.280	0.190	1075.7
2	500-1000	0.225	0.200	305.1
2	1000-500	0.245	0.180	499.7

Note: Layers indicates the number of RBMs used in the DBN. Units indicates the number of hidden units in each RBM.

in nature, and thus quite amenable to this. However, the libraries we used initially were not written in such a way as to be able to take advantage of CUDA. In order to find an effective alternative, we turned to the Python-based Theano library (`http://deeplearning.net/software/theano/`) [4]. While we were able to find appropriate Deep Learning Python scripts for the CNN and DBN, their implementation was not as advanced as the Matlab-based libraries we were already using. In particular, the DBN script did not implement Gaussian visible units. Alas, while it would have been possible to implement these ourselves, it would have required additional time and effort, and as it was already relatively late in the term, it was decided to stick with our working Matlab implementations. Perhaps in the future, for work beyond this thesis, taking advantage of the GPU by using a Theano-

Table 5.10: Early results of experiments done to test the speed of various configurations of DBNs, on the Caltech-20 using the Sylfaen lab computer, comparing Matlab versions 2009a and 2011a.

		2009a			2011a		
Parameters		Accuracy		Time (s)	Accuracy		Time (s)
Layers	Units	Non-Occluded	Occluded		Non-Occluded	Occluded	
1	100	0.125	0.165	57.4	0.125	0.165	55.7
2	100	0.280	0.185	57.9	0.280	0.185	55.7
3	100	0.160	0.150	59.6	0.160	0.150	57.5
4	100	0.120	0.110	61.0	0.120	0.110	58.2
1	200	0.160	0.130	81.2	0.160	0.130	76.6
2	200	0.235	0.140	83.8	0.235	0.140	77.4
3	200	0.175	0.165	84.4	0.175	0.165	80.3
4	200	0.160	0.175	86.3	0.160	0.175	81.9
1	500	0.220	0.120	148.5	0.220	0.120	139.7
2	500	0.220	0.150	157.0	0.220	0.150	148.5
3	500	0.175	0.115	165.6	0.175	0.115	159.9
4	500	0.170	0.115	177.2	0.170	0.115	168.1
1	1000	0.255	0.130	277.8	0.255	0.130	245.8
2	1000	0.240	0.185	302.9	0.240	0.185	276.3
3	1000	0.160	0.165	334.5	0.160	0.165	306.4
4	1000	0.165	0.160	369.0	0.165	0.160	337.5
1	1200				0.245	0.150	297.0
2	1200				0.310	0.165	329.8
1	1300				0.255	0.135	314.1
1	1500	0.250	0.135	401.1			
2	1500	0.205	0.200	449.1			

Note: Layers indicates the number of RBMs used in the DBN. Units indicates the number of hidden units in each RBM.

Table 5.11: Comparing the speed of various versions of Matlab using the Destrier laptop computer.

Matlab Version	Parameters		Accuracy		Time (s)
	Layers	Units	Non-Occluded	Occluded	
2011a 32-bit	2	1000	0.260	0.180	256.4
2011a 64-bit	2	1000	0.245	0.150	243.0
2011b 64-bit	2	1000	0.245	0.150	197.8

Note: Layers indicates the number of RBMs used in the DBN. Units indicates the number of hidden units in each RBM.

based implementation would be highly recommended, as our tests suggest that the speed of the DBN can be doubled, while the speed of the CNN could be improved by a factor of ten. The Python/Theano-based implementation performance is shown in table 5.13, table 5.14, table 5.15, table 5.16, table 5.17, and table 5.18. For comparison, the Matlab Library

Table 5.12: The results of an experiment to test the effect of hard-wired sparsity on DBNs on the Caltech-20.

Sparse Test						
Version	Parameters		Accuracy			Time (s)
	Layers	Units	Training	Non-Occluded	Occluded	
1	2	1000	0.189	0.120	0.115	658.7
1	2	2000	0.266	0.195	0.150	1350.5
			0.239	0.205	0.170	1341.0
			0.290	0.200	0.100	1401.7
1	2	3000	0.185	0.130	0.140	2275.7

Note: Layers indicates the number of RBMs used in the DBN. Units indicates the number of hidden units in each RBM.

implementation performance is shown in table 5.19 and table 5.20.

Table 5.13: Speed Tests Using Python/Theano-based DBN on MNIST

DBN - MNIST				
Computer	CPU/GPU	Speed (mins)		Theano Version
		Pre-Training	Fine-Tuning	
Panzer	GPU	112.50	19.30	0.6rc3
Panzer	CPU	197.56	44.59	0.6rc3
Destrier	GPU	172.55	34.46	0.6rc3
Destrier	CPU	313.90	509.11	0.6rc3
Panzer	GPU	111.76	18.90	bleeding edge
Panzer	CPU	195.67	44.72	bleeding edge
Destrier	CPU	293.67	481.70	bleeding edge

Note:
Computer Destrier has an Intel Core i7-2670QM 2.2 GHz processor and 16 GB of RAM.
Computer Panzer has an Intel Core i7-3770 3.4 GHz processor and 32 GB of RAM.

Table 5.14: Speed Tests Using Python/Theano-based CNN on MNIST

CNN - MNIST			
Computer	CPU/GPU	Speed (mins)	Theano Version
Panzer	CPU	406.08	0.6rc3
Panzer	GPU	38.51	bleeding edge
Panzer	CPU	405.69	bleeding edge
Destrier	GPU	98.84	bleeding edge
Destrier	CPU	562.78	bleeding edge

Note:
Computer Destrier has an Intel Core i7-2670QM 2.2 GHz processor and 16 GB of RAM.
Computer Panzer has an Intel Core i7-3770 3.4 GHz processor and 32 GB of RAM.

Finally, experiments were performed with the optimized parameters for SVMs, CNNs,

Table 5.15: Speed Tests Using Python/Theano-based DBN on Caltech-20

DBN - Caltech20							
Computer	CPU/GPU	Speed		Best Validation Score	Test Performance		Theano Version
		Pre-Training	Fine-Tuning		Error	Accuracy	
Panzer	CPU	59.15 mins	84.20 mins	0.00%	63.50%	36.50%	bleeding edge
Panzer	GPU	14.26 mins	15.89 mins	0.00%	67.50%	32.50%	bleeding edge

Note: Computer Panzer has an Intel Core i7-3770 3.4 GHz processor and 32 GB of RAM.

Table 5.16: Speed Tests Using Python/Theano-based CNN on Caltech-20

CNN - Caltech20						
Computer	CPU/GPU	Speed (mins)	Best Validation Score	Test Performance		Theano Version
				Error	Accuracy	
Panzer	CPU	37.60	23.40%	nan%		bleeding edge
Panzer	GPU	4.07	19.40%	nan%		bleeding edge
Panzer	GPU	5.24	0.00%	47.50%	52.50%	bleeding edge
Panzer	CPU	43.17	0.00%	50.50%	49.50%	bleeding edge

Note: Computer Panzer has an Intel Core i7-3770 3.4 GHz processor and 32 GB of RAM.

and DBNs on the Caltech-101 and small NORB image datasets, once again with non-occluded and occluded image sets as seen in figure 5.3 and figure 5.4 respectively. As with the Caltech-20, these experiments consisted of three different methods of training: one which consisted of training exclusively on the non-occluded training set of non-occluded images, followed by testing on both a non-occluded test set and an occluded test set; one which consisted of training on a mixture of non-occluded and occluded images, followed by testing on both a non-occluded test set and an occluded test set; and finally one which consisted of training exclusively on the occluded training set, followed by testing on both a non-occluded test set and an occluded test set.

Table 5.17: Speed Tests Using Python/Theano-based DBN on NORB

DBN - NORB							
Computer	CPU/GPU	Speed (mins)		Best Validation Score	Test Performance		Notes
		Pre-Training	Fine-Tuning		Error	Accuracy	
Panzer	CPU	1674.53	191.76	40.56%	46.24%	53.76%	default
Panzer	GPU	650.28	35.96	47.28%	52.80%	47.20%	default
Panzer	GPU	495.24	85.14	20.00%	37.50%	62.50%	2 layers
Panzer	GPU	492.70	2738.09	0.24%	19.35%	80.65%	0.001 learning rate, 1000 epochs fine
Panzer	GPU	985.71	146.39	16.05%	27.24%	72.76%	200 epochs pre 50 epochs fine
Panzer	GPU	248.87	11.49	59.34%	59.63%	40.37%	100 epochs fine, batch size 100
Panzer	GPU	125.01	1.72	66.89%	68.22%	31.78%	100 epochs pre, 100 epochs fine, batch size 100
Panzer	GPU	250.19	22.22	42.47%	49.41%	50.59%	200 epochs pre 100 epochs fine, batch size 100
Panzer	GPU	250.26	1.96	67.38%	67.12%	32.88%	ditto

Note: Variation in Fine-Tuning times may be due to early-stopping. Computer Panzer has an Intel Core i7-3770 3.4 GHz processor and 32 GB of RAM.

Table 5.18: Speed Tests Using Python/Theano-based CNN on NORB

CNN - NORB						
Computer	CPU/GPU	Speed (mins)	Best Validation Score	Test Performance		Notes
				Error	Accuracy	
Panzer	CPU	49.51	80.00%	80.00%	20.00%	
Panzer	GPU	6.34	80.00%	80.00%	20.00%	
Destrier	CPU	69.18	62.67%	61.63%	38.37%	
Destrier	GPU	27.53	77.76%	77.23%	22.77%	
Destrier	GPU	33.30	0.86%	17.30%	82.70%	0.01 learning rate
Destrier	GPU	31.48	79.43%	79.34%	20.66%	0.00002 learning rate
Destrier	GPU	300.17	0.48%	17.96%	82.04%	0.001 learning rate
Destrier	GPU	318.07	3.74%	20.55%	79.45%	0.0001 learning rate
Destrier	GPU	257.92	3.65%	21.21%	78.79%	0.001 learning rate, batch size 100
Destrier	GPU	243.98	0.00%	16.31%	83.69%	0.01 learning rate, batch size 100
Destrier	GPU	244.74	0.32%	17.39%	82.61%	0.01 learning rate, batch size 100
Destrier	GPU	247.97	0.05%	18.33%	81.67%	ditto

Note: Variation in times may be due to early-stopping.
Computer Destrier has an Intel Core i7-2670QM 2.2 GHz processor and 16 GB of RAM.
Computer Panzer has an Intel Core i7-3770 3.4 GHz processor and 32 GB of RAM.

Table 5.19: Results and Times for CNN trained on Non-Occluded dataset of NORB for 100 Epochs Using Matlab Library.

Matlab: DBN - NORB							
Accuracy Results				Time To Train			
Train	Test	Non-Occluded	Occluded	Seconds	Minutes	Hours	Days
0.985	0.505	0.801	0.208	32548.6	542.48	9.041	0.3767

Table 5.20: Results and Times for CNN trained on Non-Occluded dataset of NORB for 100 Epochs Using Matlab Library.

Matlab: CNN - NORB							
Accuracy Results				Time To Train			
Train	Test	Non-Occluded	Occluded	Seconds	Minutes	Hours	Days
0.955		0.831	0.199	177997.1	2966.62	49.444	2.0602
0.955	0.515	0.831	0.199	178195.3	2969.92	49.499	2.0624
0.955	0.515	0.831	0.199	179563.8	2992.73	49.879	2.0783
0.955	0.515	0.831	0.199	181078.3	3017.97	50.300	2.0958
0.955	0.515	0.831	0.199	181197.2	3019.95	50.333	2.0972

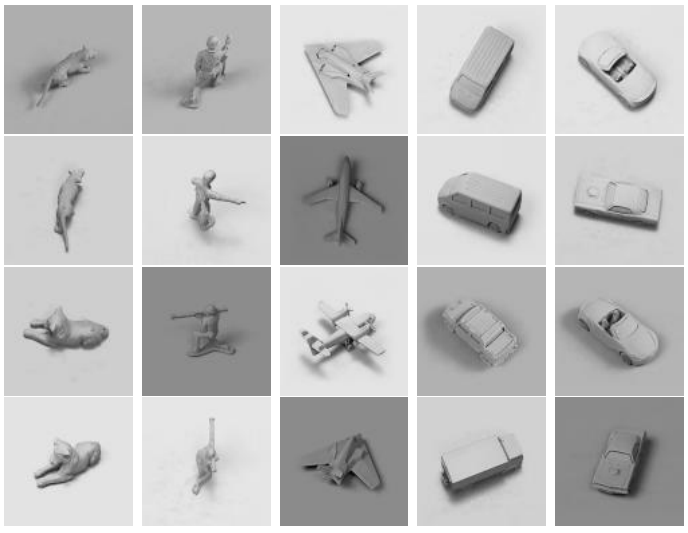

Figure 5.3: Images from the small NORB non-occluded test set.

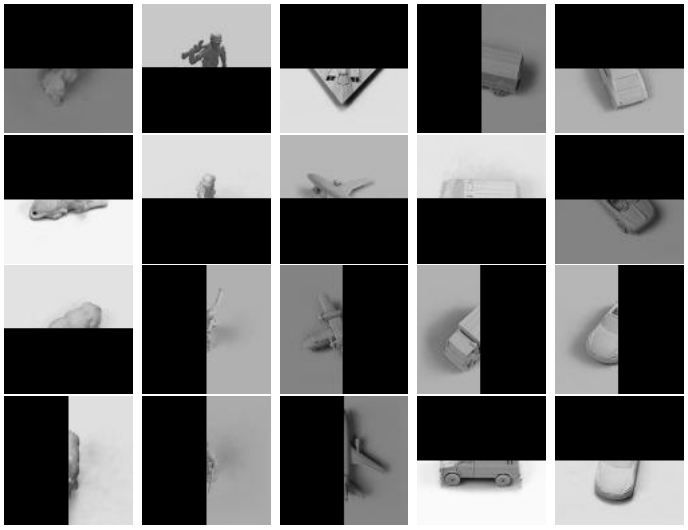

Figure 5.4: Images from the small NORB occluded test set.

Chapter 6

Analysis and Results

The performance of machine learning algorithms in recognizing the object in an occluded image depends on the method of training. The training process can consist of various data sets, ranging from one made up exclusively of non-occluded images, to one made up exclusively of occluded images, and also various mixtures of the two. The fully trained algorithm can then be tested in terms of accuracy on both non-occluded images, and occluded images. A further testing set containing a mixture of non-occluded and occluded images can also be used.

6.1 Results on NORB

6.1.1 Support Vector Machines

Table 6.1 provides a direct comparison of the non-occluded, occluded, and mixed trained SVMs. The original raw data can be found in Appendix A. The results show that when the SVM is trained with only non-occluded training images, its object recognition performance

on non-occluded test images is reasonably good (83% accuracy), but the same algorithm performs poorly on the occluded test images (20% accuracy). On the other hand, when the SVM is trained with only occluded training images, it performs reasonably well at object recognition on the occluded test images (69% accuracy), but performs poorly on the non-occluded test images (20% accuracy).

The results also showed that training the SVM on the mixed data set containing both non-occluded and occluded images, led it to do well at object recognition on the non-occluded test images (81% accuracy), on the occluded test images (69% accuracy), and also on the mixed test images (75% accuracy). These accuracies on the non-occluded test images are comparable to the SVMs trained on the non-occluded training images (i.e., 81% vs. 83%). Furthermore, its accuracy on the occluded test images is comparable to the SVMs trained on the occluded training images (i.e., 69% vs. 69%).

When comparing performance on the mixed test data set, the SVM performed better if trained with the mixed training data set (75% accuracy), than if it was trained using the non-occluded training images (51% accuracy), or the occluded training images (45% accuracy) alone.

When testing the SVM on the same training data set as it was trained on, the accuracy on the object recognition task was slightly lower when using the mixed training images (97% accuracy) than if it was trained exclusively on the non-occluded training images (99.9% accuracy), or exclusively on the occluded training images (99% accuracy). To understand this, the concept of overfitting must be considered. Overfitting occurs when a learning algorithm learns to fit itself to the training data, rather than learning the general concept that it is desired to learn from the training data. In such an instance, the performance on the test data can actually decrease while accuracy on the original training data continues to increase. Obviously, performance on the original training data should be better than performance on previously unseen test data, but it is possible that if the difference between

the two performances is significant, this could indicate some degree of overfitting.

Table 6.1: A comparison of the accuracy results of the non-occluded, occluded, and mixed trained SVMs on the NORB dataset.

Training	Training Test	Mixed Test	Non-Occluded Test	Occluded Test
Non-Occluded	0.999 ± 0.003	0.513 ± 0.001	0.825 ± 0.007	0.200 ± 0.003
Occluded	0.994 ± 0.0001	0.446 ± 0.0002	0.200 ± 0.0001	0.692 ± 0.0005
Mixed	0.973 ± 0.0003	0.754 ± 0.001	0.813 ± 0.001	0.694 ± 0.0005

Note: Mean of 3 replicates $\pm$ standard error.

6.1.2 Convolutional Neural Networks

Table 6.2 provides a direct comparison of the non-occluded, occluded, and mixed trained CNNs. The original raw data can be found in Appendix A. The results show that when the CNN is trained with only non-occluded training images, its object recognition performance on non-occluded test images is reasonably good (83% accuracy), but the same algorithm performs poorly on the occluded test images (20% accuracy). On the other hand, when the CNN is trained with only occluded training images, it performs reasonably well at object recognition on the occluded test images (59% accuracy), but performs poorly on the non-occluded test images (30% accuracy), albeit notably better than the equivalent SVM.

The results also showed that training the CNN on the mixed data set containing both non-occluded and occluded images, led it to do well at object recognition on the non-occluded test images (77% accuracy), on the occluded test images (67% accuracy), and also on the mixed test images (72% accuracy). This accuracy on the non-occluded test images is comparable to the CNNs trained on the non-occluded training images (i.e., 77% vs. 83%). Furthermore, the mixed trained CNN's accuracy on the occluded test images is notably better than the CNNs trained on the occluded training images (i.e., 67% vs. 59%).

When comparing performance on the mixed test data set, the CNN performed better if trained with the mixed training data set (72% accuracy), than if trained with the occluded training images (44% accuracy) alone.

When testing the CNN on the same training data set as it was trained on, the accuracy on the object recognition task was significantly lower when using the mixed training images (83% accuracy) than if it was trained exclusively on the non-occluded training images (96% accuracy). Testing on the occluded training images actually had the lowest performance of the three options (69% accuracy). It is possible that this suggests that there was less overfitting on mixed and occluded training images than on the non-occluded training images.

Table 6.2: A comparison of the accuracy results of the non-occluded, occluded, and mixed trained CNNs on the NORB dataset.

Training	Training Test	Mixed Test	Non-Occluded Test	Occluded Test
Non-Occluded	0.955 ± 0.000	0.515 ± 0.000	0.831 ± 0.000	0.199 ± 0.000
Occluded	0.693 ± 0.003	0.444 ± 0.017	0.304 ± 0.031	0.585 ± 0.002
Mixed	0.832 ± 0.002	0.717 ± 0.003	0.769 ± 0.009	0.665 ± 0.010

Note: Mean of 3 replicates $\pm$ standard error.

6.1.3 Deep Belief Networks

Table 6.3, table 6.4, and table 6.5 provide a direct comparison of the non-occluded, occluded, and mixed trained DBNs, with the differences between each table resulting from the effects of choosing different visible units and number of hidden units in the ANN.

Table 6.3 shows specifically the performance of the DBNs using binary visible units and having 2000 hidden nodes. As expected, the DBN trained on the non-occluded training images achieves a respectable performance (87% accuracy) on the non-occluded test images, while not performing so well on the occluded test images (21% accuracy). Conversely, the DBN trained on the occluded training images managed to achieve reasonably good results on the occluded test images (71% accuracy), while not fairing so well on the non-occluded test images (19% accuracy).

The DBN trained on the mixed training images managed a somewhat lower performance on the non-occluded test set than the DBN trained exclusively on the non-occluded training images (68% vs. 87% accuracy), and a slightly lower performance on the occluded

test set than the DBN trained exclusively on the occluded training images (68% vs. 71% accuracy).

When comparing performance on the mixed test data set, the DBN performed better if trained with the mixed training data set (68% accuracy), than if it was trained using the occluded training images (45% accuracy) alone.

When testing the DBN on the same training data set as it was trained on, the accuracy on the object recognition task was significantly lower when using the mixed training images (83% accuracy) or the occluded training images (85% accuracy), than if it was trained exclusively on the non-occluded training images (99% accuracy).

Table 6.3: A comparison of the accuracy results of the non-occluded, occluded, and mixed trained DBNs using binary visible units with 2000 hidden nodes.

DBN - Binary Visible Unit w/ 2000 Hidden Nodes				
Training	Training Test	Mixed Test	Non-Occluded Test	Occluded Test
Non-Occluded	0.993 ± 0.0002	0.545 ± 0.000	0.873 ± 0.007	0.214 ± 0.004
Occluded	0.847 ± 0.007	0.451 ± 0.026	0.193 ± 0.044	0.708 ± 0.009
Mixed	0.832 ± 0.013	0.680 ± 0.013	0.676 ± 0.037	0.684 ± 0.020

Note: Mean of 3 replicates $\pm$ standard error.

Table 6.4 shows specifically the performance of the DBNs using binary visible units and having 4000 hidden nodes. As expected, the DBN trained on the non-occluded training images achieves a respectable performance (84% accuracy) on the non-occluded test images, while not performing so well on the occluded test images (20% accuracy). Conversely, the DBN trained on the occluded training images managed to achieve reasonably good results on the occluded test images (71% accuracy), while not fairing so well on the non-occluded test images (21% accuracy).

The DBN trained on the mixed training images managed a somewhat lower performance on the non-occluded test set than the DBN trained exclusively on the non-occluded training images (65% vs. 84% accuracy), and a slightly lower performance on the occluded test set than the DBN trained exclusively on the occluded training images (69% vs. 71%

accuracy).

When comparing performance on the mixed test data set, the DBN performed better if trained with the mixed training data set (67% accuracy), than if it was trained using the occluded training images (46% accuracy) alone.

When testing the DBN on the same training data set as it was trained on, the accuracy on the object recognition task was significantly lower when using the mixed training images (87% accuracy) or the occluded training images (85% accuracy), than if it was trained exclusively on the non-occluded training images (99% accuracy).

Table 6.4: A comparison of the accuracy results of the non-occluded, occluded, and mixed trained DBNs using binary visible units with 4000 hidden nodes.

DBN - Binary Visible Unit w/ 4000 Hidden Nodes				
Training	Training Test	Mixed Test	Non-Occluded Test	Occluded Test
Non-Occluded	0.989 ± 0.002	0.520 ± 0.008	0.841 ± 0.014	0.203 ± 0.002
Occluded	0.852 ± 0.007	0.458 ± 0.014	0.208 ± 0.022	0.708 ± 0.006
Mixed	0.866 ± 0.008	0.673 ± 0.001	0.653 ± 0.004	0.693 ± 0.004

Note: Mean of 3 replicates ± standard error.

Table 6.5 shows specifically the performance of the DBNs using Gaussian visible units and having 4000 hidden nodes. As expected, the DBN trained on the non-occluded training images achieves a respectable performance (83% accuracy) on the non-occluded test images, while not performing so well on the occluded test images (26% accuracy). Conversely, the DBN trained on the occluded training images managed to achieve reasonably good results on the occluded test images (65% accuracy), while also doing quite well on the non-occluded test images (69% accuracy). This discovery of better performance when trained with occluded images and tested with non-occluded images in G-4000 could be due to the generative model's ability to learn to classify whole images using features learned from the partial images of the occluded images.

The DBN trained on the mixed training images managed a somewhat lower performance on the non-occluded test set than the DBN trained exclusively on the non-occluded

training images (71% vs. 83% accuracy), and a slightly higher performance on the occluded test set than the DBN trained exclusively on the occluded training images (68% vs. 65% accuracy). This superior performance by the mixed trained SVM on the occluded test set was unexpected, and could be due to the larger size of the mixed training data set, which essentially includes all the images from the non-occluded training data set, and all the images from the occluded training data set.

When comparing performance on the mixed test data set, the DBN performed better if trained with the mixed training data set (70% accuracy), than if it was trained using the occluded training images (67% accuracy) alone.

When testing the DBN on the same training data set as it was trained on, the accuracy on the object recognition task was significantly lower when using the mixed training images (86% accuracy) or the occluded training images (79% accuracy), than if it was trained exclusively on the non-occluded training images (98% accuracy).

Table 6.5: A comparison of the accuracy results of the non-occluded, occluded, and mixed trained DBNs using Gaussian visible units with 4000 hidden nodes.

DBN - Gaussian Visible Unit w/ 4000 Hidden Nodes				
Training	Training Test	Mixed Test	Non-Occluded Test	Occluded Test
Non-Occluded	0.981 ± 0.003	0.550 ± 0.002	0.832 ± 0.006	0.258 ± 0.013
Occluded	0.786 ± 0.001	0.673 ± 0.002	0.693 ± 0.006	0.652 ± 0.005
Mixed	0.860 ± 0.016	0.697 ± 0.023	0.714 ± 0.044	0.679 ± 0.006

Note: Mean of 3 replicates ± standard error.

6.1.4 Comparison

Table 6.6 compares the various classification algorithms that have been trained on the non-occluded images. As expected, the performance on the non-occluded test images is reasonably high (83-87% accuracy). Conversely performance on the occluded test images is expectedly poor (20-26% accuracy).

Performance on the mixed test images appears to be the average of the non-occluded and occluded test image performances (51-55% accuracy).

Performance on the original training images is very high across the board (96-99% accuracy).

Table 6.6: Comparison of the accuracy results of the Classifier Algorithms on the Non-Occluded Training Images

Trained On Non-Occluded Training Image Set				
Classifier	Training Test	Mixed Test	Non-Occluded Test	Occluded Test
SVM	**0.999 ± 0.003**	0.513 ± 0.001	0.825 ± 0.007	0.200 ± 0.003
CNN	0.955 ± 0.000	0.515 ± 0.000	0.831 ± 0.000	0.199 ± 0.000
DBN (B-2000)	0.993 ± 0.0002	0.545 ± 0.000	**0.873 ± 0.007**	0.214 ± 0.004
DBN (B-4000)	0.989 ± 0.002	0.520 ± 0.008	0.841 ± 0.014	0.203 ± 0.002
DBN (G-4000)	0.981 ± 0.003	**0.550 ± 0.002**	0.832 ± 0.006	**0.258 ± 0.013**

Note: Mean of 3 replicates ± standard error. Highest value per test type shown in bold face.

Table 6.7 compares the various classification algorithms that have been trained on the occluded images. While the SVM, DBN (B-2000), and the DBN (B-4000) achieve around chance on the non-occluded test images (19-21% accuracy), the CNN achieves a somewhat higher than chance result (30% accuracy), and the DBN (G-4000) achieves a remarkably high result (69% accuracy). These results are unusual because one would expect that classifiers trained on the occluded test set exclusively might perform at chance on the non-occluded test set (20% accuracy). However, several of the algorithms used achieved significantly higher numbers on a test set type that it wasn't trained on. This suggests that learning the occluded set is actually sometimes useful to classifying on the non-occluded set. Meanwhile, the performance on the occluded test images is closer to expected (59-71% accuracy).

Performance on the mixed test images appears to be the average of the non-occluded and occluded test image performances (44-67% accuracy).

Performance on the original training images is more varied than with the non-occluded

(69-99% accuracy), though still consistently higher than performance on the test images.

Table 6.7: Comparison of the accuracy results of the Classifier Algorithms on the Occluded Training Images

Trained On Occluded Training Image Set				
Classifier	Training Test	Mixed Test	Non-Occluded Test	Occluded Test
SVM	**0.994 ± 0.0001**	0.446 ± 0.0002	0.200 ± 0.0001	0.692 ± 0.0005
CNN	0.693 ± 0.003	0.444 ± 0.017	0.304 ± 0.031	0.585 ± 0.002
DBN (B-2000)	0.847 ± 0.007	0.451 ± 0.026	0.193 ± 0.044	**0.708 ± 0.009**
DBN (B-4000)	0.852 ± 0.007	0.458 ± 0.014	0.208 ± 0.022	**0.708 ± 0.006**
DBN (G-4000)	0.786 ± 0.001	**0.673 ± 0.002**	**0.693 ± 0.006**	0.652 ± 0.005

Note: Mean of 3 replicates ± standard error. Highest value per test type shown in bold face.

Table 6.8 compares the various classification algorithms that have been trained on the mixed image set. As expected, the performance on the non-occluded test images is reasonable (65-81% accuracy), albeit within a significantly wider range than the performance on the occluded test images (67-69% accuracy).

Performance on the mixed test images appears to be the average of the non-occluded and occluded test image performances (67-75% accuracy).

Performance on the original training images (83-97% accuracy) is lower than with the non-occluded images though less varied than the occluded images, and it remains consistently higher than performance on the test images.

Table 6.8: Comparison of the accuracy results of the Classifier Algorithms on the Mixed Training Images

Trained On Mixed Training Image Set				
Classifier	Training Test	Mixed Test	Non-Occluded Test	Occluded Test
SVM	**0.973 ± 0.0003**	**0.754 ± 0.001**	**0.813 ± 0.001**	**0.694 ± 0.0005**
CNN	0.832 ± 0.002	0.717 ± 0.003	0.769 ± 0.009	0.665 ± 0.010
DBN (B-2000)	0.832 ± 0.013	0.680 ± 0.013	0.676 ± 0.037	0.684 ± 0.020
DBN (B-4000)	0.866 ± 0.008	0.673 ± 0.001	0.653 ± 0.004	0.693 ± 0.004
DBN (G-4000)	0.860 ± 0.016	0.697 ± 0.023	0.714 ± 0.044	0.679 ± 0.006

Note: Mean of 3 replicates ± standard error. Highest value per test type shown in bold face.

6.1.5 Visualizations

A way to understand why there was such differences between the different types of DBNs is to look at the pre-trained and fine-tuned weights and their differences. It can be useful to compare these visualizations with the visualizations in different cases, along each column. Figures 6.1, 6.2, and 6.3 show a visualization of the weights of DBNs trained on non-occluded data.

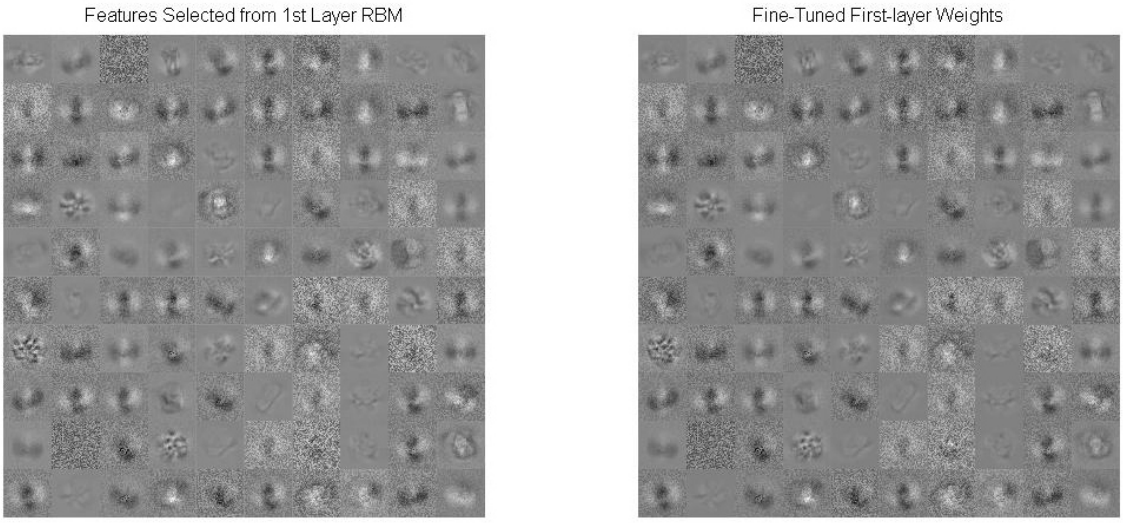

Figure 6.1: A visualization of the first layer weights of a DBN with binary visible units and 2000 hidden nodes, trained on non-occluded NORB data.

Figures 6.4, 6.5, and 6.6 show a visualization of the weights of DBNs trained on occluded data. Here the binary visible units seem to tend to create much more blacked out regions than the Gaussian visible units. The Gaussian visible unit based DBN on the other hand looks much more similar to DBNs trained on the non-occluded or mixed data. This perhaps helps to explain why the Gaussian visible unit based DBN performs so much better on the non-occluded and mixed test sets, despite being trained on occluded images only.

Figures 6.7, 6.8, and 6.9 show a visualization of the weights of DBNs trained on mixed data.

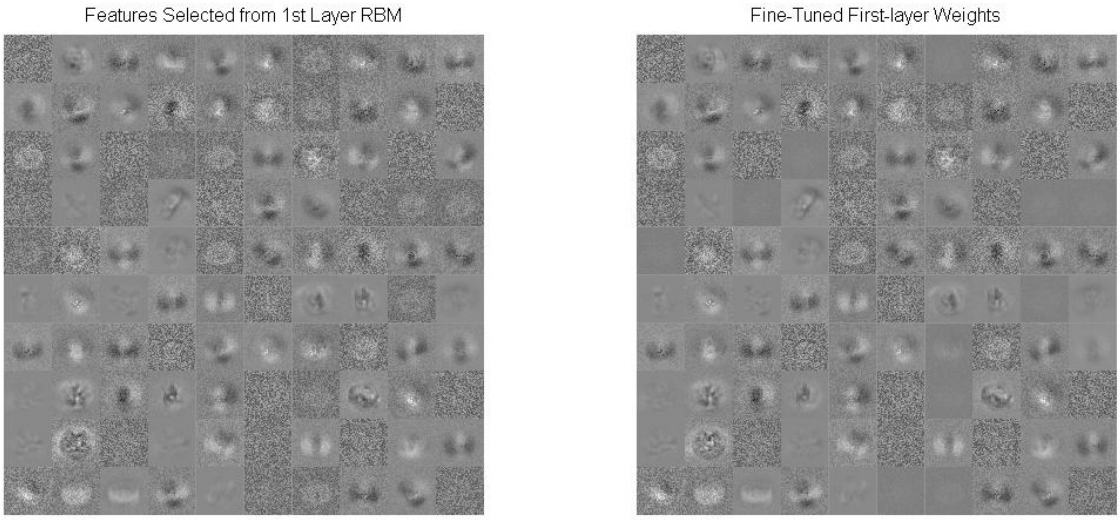

Figure 6.2: A visualization of the first layer weights of the DBN with binary visible units and 4000 hidden nodes, trained on non-occluded NORB data.

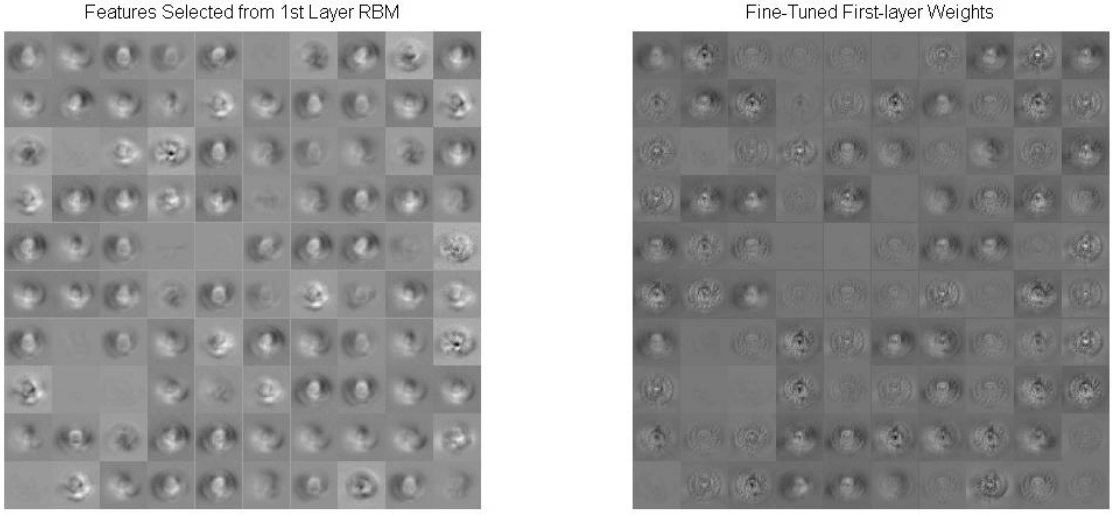

Figure 6.3: A visualization of the first layer weights of the DBN with Gaussian visible units and 4000 hidden nodes, trained on non-occluded NORB data.

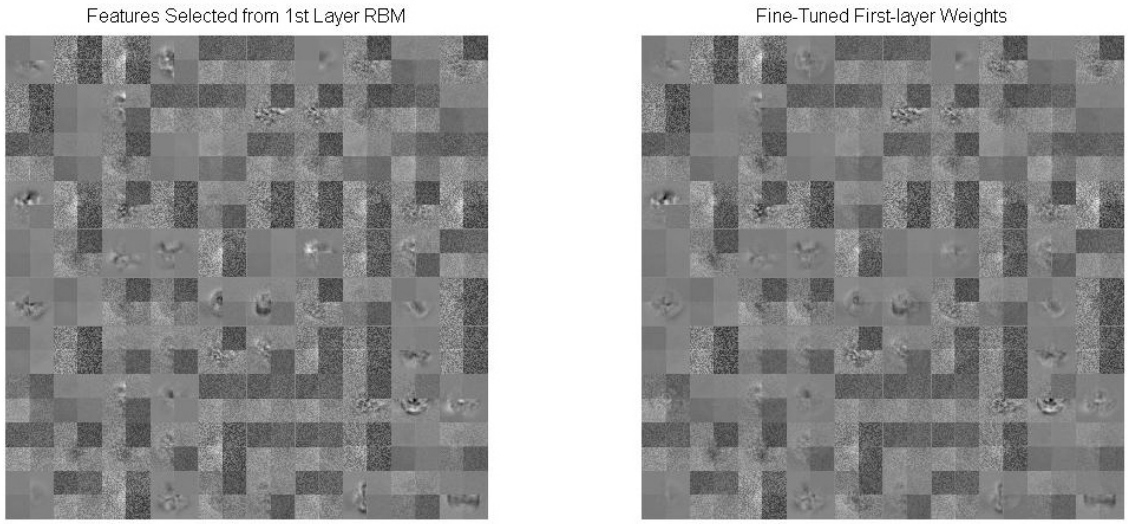

Figure 6.4: A visualization of the first layer weights of a DBN with binary visible units and 2000 hidden nodes, trained on occluded NORB data.

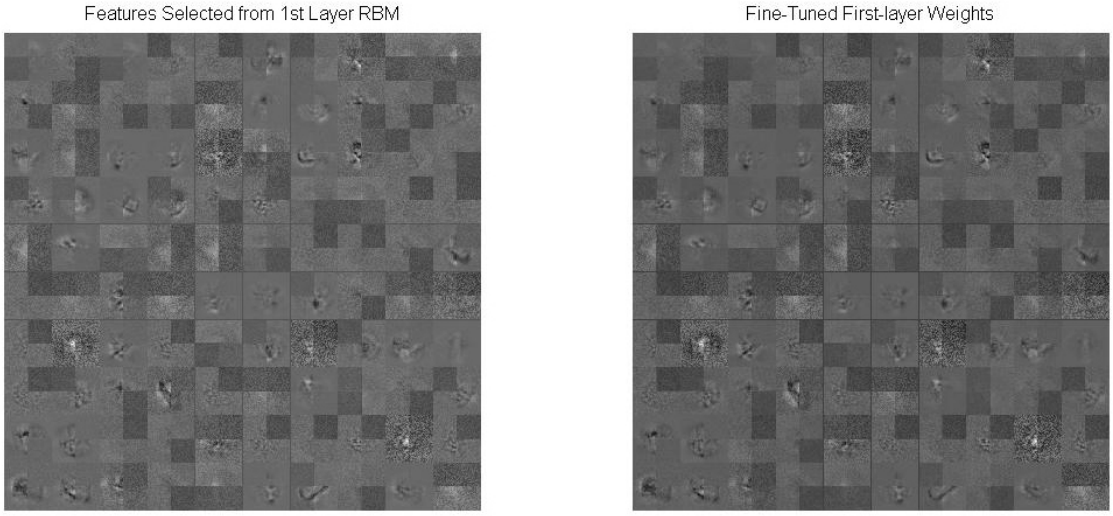

Figure 6.5: A visualization of the first layer weights of the DBN with binary visible units and 4000 hidden nodes, trained on occluded NORB data.

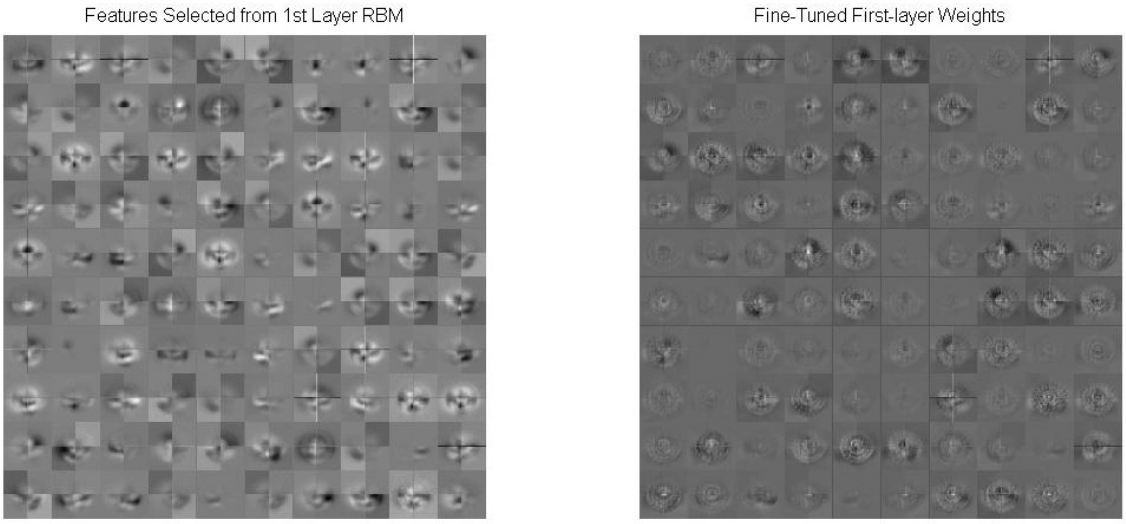

Figure 6.6: A visualization of the first layer weights of the DBN with Gaussian visible units and 4000 hidden nodes, trained on occluded NORB data.

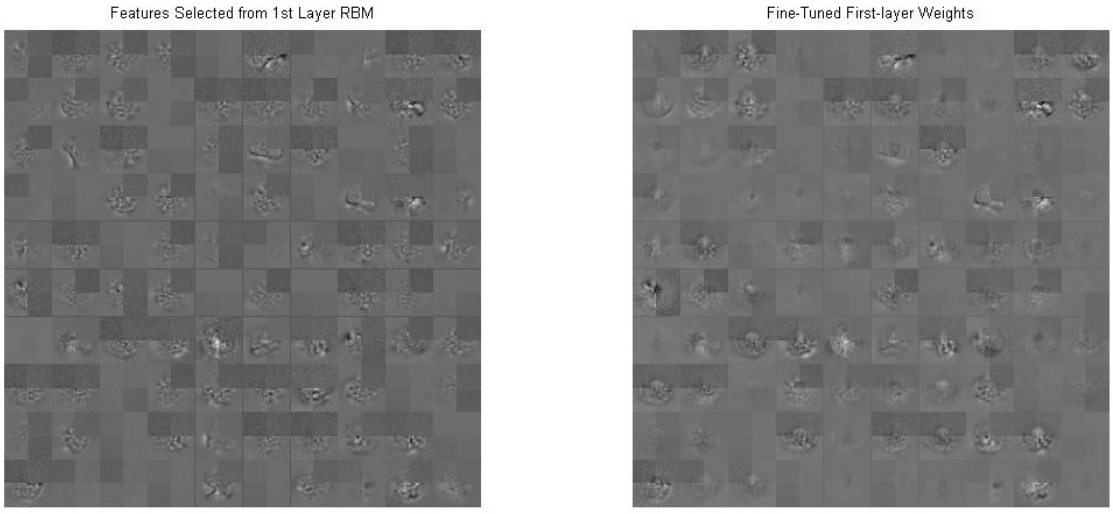

Figure 6.7: A visualization of the first layer weights of a DBN with binary visible units and 2000 hidden nodes, trained on mixed NORB data.

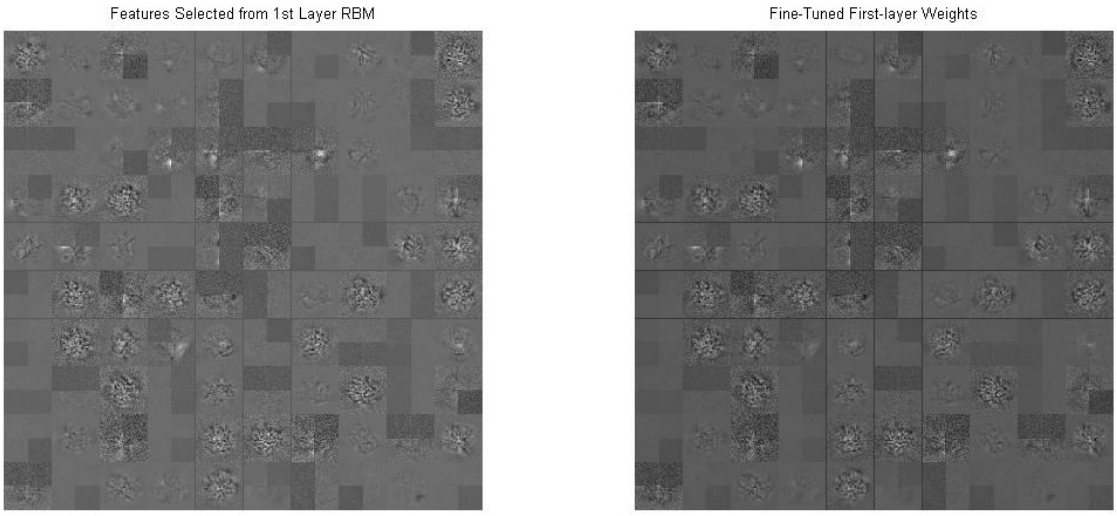

Figure 6.8: A visualization of the first layer weights of the DBN with binary visible units and 4000 hidden nodes, trained on mixed NORB data.

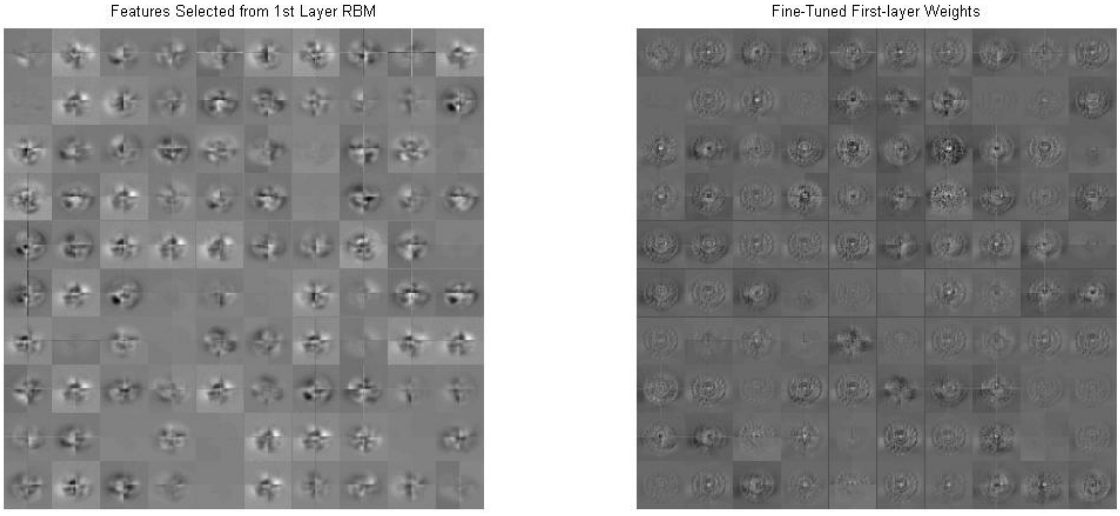

Figure 6.9: A visualization of the first layer weights of the DBN with Gaussian visible units and 4000 hidden nodes, trained on mixed NORB data.

Chapter 7

Discussion

The experiments performed have shown that when training a classifier on only the non-occluded training set, the occluded task is a particularly challenging one for both the discriminative models, such as SVMs and CNNs, and the generative models, namely the DBNs. In general, training on the non-occluded images tends to lead to good performance on the non-occluded test set, but poor performance on the occluded test set, while in most cases, training on the occluded images leads to good performance on the occluded test set, and poorer performance on the non-occluded test set.

However, it appears that training on the occluded training set only, for DBNs using Gaussian visible units at least, produces a highly unusual result of good performance on the non-occluded test set (69% accuracy). This behaviour is not apparent with the DBN using binary visible units (19-21% accuracy). A much less pronounced but similar effect is also visible with the CNN (30% accuracy), which is not seen at all with SVM, which performs at chance (20% accuracy). It may be that this is because the SVM is a purely discriminative model. The CNN while also a discriminative model, is also an ANN, which gives it some similarity to the DBN. Nevertheless, the unexpectedly good performance of

the Gaussian visible unit based DBN on the dataset type it wasn't trained on is something perhaps worth looking into for future research. Though this seems to come at a cost to performance on occluded test set, as it is the only classifier that performs better on the dataset type it wasn't trained on (69% accuracy), than on the type it was trained on (65% accuracy).

Training the SVM, the CNN, and the DBN with Gaussian visible units on a mixed training set containing both non-occluded and occluded images leads to slightly worse performance on the non-occluded test set than an exclusively non-occluded trained classifier, and slightly better performance on the occluded test set than an exclusively occluded trained classifier. This result suggests that mixed training actually improves performance on the occluded problem. It is possible that these classifiers are benefiting from the more complete images in the non-occluded part of the training set.

Training a DBN with binary visible units on a mixed training set containing both non-occluded and occluded images performs worse on the non-occluded test set than a pure non-occluded training set, and is worse but is very close in performance on the occluded test set to that trained on a pure occluded training set. This is expected, as a mixed training set should yield mediocre performance on both test sets compared to classifiers trained exclusively on the non-occluded or the occluded training sets.

While training a SVM, CNN, and a DBN with Gaussian visible units on a mixed training set leads to better relative performance on the non-occluded test image set than on the occluded test image set, the reverse appears to be the case with DBNs with binary visible units, which had better relative performance on the occluded test image set than on the non-occluded test image set. This is somewhat curious, and may be indicative of the differences between binary and Gaussian visible units.

In comparison to other work in the literature, the experiments performed on the

SVM and CNN did not exceed the performance of the results from Huang and LeCun [26]. Huang and LeCun were able to achieve 88.4% accuracy with their SVM on the small NORB dataset, and 93.8% accuracy with their CNN on the small NORB dataset. The SVM in our experiments, with the same parameters as Huang and LeCun, achieved $82.5\% \pm 0.7\%$ accuracy, while our CNN achieved 83.1% accuracy. Our best performing algorithm was actually a DBN using binary visible units and 2000 hidden nodes, which achieved 87% accuracy. In comparison, Nair and Hinton [37], achieved 93.5% accuracy with their DBN on the standard small NORB dataset, and 94.8% accuracy with their DBN using extra unlabeled data. Thus, on the non-occluded or non-occluded images, we did not achieve quite as good results as the best in the literature, as shown in table 7.1.

Table 7.1: Comparison of the accuracy results of the Classifier Algorithms with those in the literature on NORB

Trained On Unoccluded NORB Images and Tested on Unoccluded NORB Images	
Classifier	Accuracy
Our SVM	0.825 ± 0.007
SVM from Huang and LeCun [26]	0.884
Our CNN	0.831 ± 0.000
CNN from Huang and LeCun [26]	0.938
Our DBN (B-2000)	0.873 ± 0.007
Our DBN (B-4000)	0.841 ± 0.014
Our DBN (G-4000)	0.832 ± 0.006
DBN from Nair and Hinton [37]	0.935

Note: Mean of 3 replicates ± standard error.

A major reason for our relatively inferior performance was that we chose to only take one of the two stereo images in the NORB dataset to be used by our algorithms. The top performing results in the literature on the other hand, generally made use of both of the stereo images. We chose not to use the stereo pair images primarily because of limitations on our part, namely that it would double the size of the dataset in memory, and that in the case of the CNN it would require a considerable modification to the architecture of the network. Thus, we chose to save both memory and time by using only the single image. This was an important choice, because we were limited in the amount of RAM available on our computers, and the amount of time to required to train with even this limited version

of the NORB was quite substantial. Also, in reality it often difficult to obtain stereo images without resorting to some special robotic vision setup. Conversely, single images are readily available in many datasets, CCTV cameras, and Internet searches.

As far as occluded images are concerned, there is a lack of results in the literature that are directly comparable to our work. Probably the most similar work done so far would be Ranzato et al. [44]. Their work on classifying facial expressions includes some use of occlusion. Rather than using NORB, they used the Cohn-Kanade (CK) dataset, and the Toronto Face Database (TFD), classifying 7 different facial expressions, rather than 5 objects. Their Type 3 - right half, Type 4 - bottom half, and Type 5 - top half occlusions are most similar to the occlusions we used in our experiments. Unlike our experiments, their deep generative model actually attempts to reconstruct the image first before classifying. This takes full advantage of the unique properties of generative models. As such, they achieve fairly impressive results, as shown in Figure 7 of Ranzato et al. [44], and Figure 8 of Ranzato et al. [44].

The top graphs of both of these figures show the results when only test images are occluded. This is would be equivalent to our performance seen in column five of table 6.6, where the classifiers are trained on the non-occluded, and tested on the occluded images. Similarly to what we found in our own experiments, Ranzato et al. [44] found this to be the more difficult task for most models than the alternative of training on occluded images and testing on occluded images.

The bottom graphs of both of these figures show the results when both training and test images are occluded. This is would be equivalent to our performance seen in column five of table 6.7, where the classifiers are trained on the occluded, and tested on the occluded images. Similarly to what we found in our own experiments, Ranzato et al. [44] found this to be an easier task for most models than training on the non-occluded images and testing on the occluded images.

Overall these figures in combination with our own results appear to show that the advantage of using a generative model comes from the reconstruction process that Ranzato et al. [44] were able to use, and is not simply a result of classification using a generative model discriminatively as we did. Further research naturally could involve actually implementing some kind of reconstruction process similar to what Ranzato et al. [44] used, except on the small NORB dataset, to see whether or not this conjecture actually holds.

A further possible reason why the performance of the generative DBN did not exceed the discriminative models could be because the DBNs were fine-tuned with Backpropagation. As this process is inherently discriminative rather than generative, the final resulting network perhaps behaves more like a discriminative model than a generative model. If this is the case, we should be able to see some difference in the accuracy of the model when it has only been pre-trained, and not yet fine-tuned with Backpropagation. Looking at Appendix table A.7 we see that the pre-fine-tuning performance of a DBN trained on the non-occluded dataset, and tested on the occluded data is comparable to that after fine-tuning with Backpropagation. To truly test this possibility, we may need to find a generative model that is fully generative through and through, such as a DBM.

We did run some experiments with more complicated occlusions than merely the four half-planes that we used in the main experiment, but it was found that for the most part, performance was related mainly to what percentage of the actual object was occluded by the occlusions. Things like moving the occlusion across the image, only led to increasing this percentage of occlusion and generally reducing performance.

Also, the features that our algorithms used were selected by the algorithm through learning, and so it is possible that incorporating preprocessing or feature extracting layers for features that would be useful in spite of the occlusions, such as texture, might in theory improve performance, though it should be said that the value of most of these algorithms is in their ability to determine their own features through learning.

Our experiments involved a significant amount of searching for ideal hyper-parameters for various configurations of the various algorithms. Much of the work was done by manually tuning these hyper-parameters and exhaustively searching for the best values. Some efficiency could possibly be introduced by a method of automatic parameter setting, that would involve using scripts to exhaustively search possible configurations. However, as most of the time involved in the exhaustive searches was in the actual running of the various configurations, it would probably have a minimal overall impact.

Future work may include experiments on other data sets, such as the Caltech-101 proper, which would allow us to be more certain that the findings of our previous experiments hold for data sets other than just NORB. We could also look at using more generative reconstruction techniques with the DBN, to see whether or not the extra stage that Ranzato et al. [44] used can be performed using the regular DBN architecture, rather than their Deep Generative Model. Other future research might also include testing different types of occlusions than the ones we used, to see whether or not that could make a difference, and to what degree.

As mentioned in Chapter 3, there is also possible as a future research direction, the possibility of additional efforts to optimize the hyper-parameters of the CNN, such as additional work to clarify the number of feature maps considerations, as well as perhaps determining the optimal receptive field size, and also the optimal number of layers. Given it is uncertain how much these hyper-parameters depend on a particular data set, so running some of the previous experiments using other data sets than the Caltech-20, such as on NORB or the Caltech-101 proper, could yield some interesting results. Furthermore, an effort into seeing whether or not a more useful measure of spatial entropy can be found could also be considered.

Chapter 8

Conclusions

Our experiments with the CNN, in attempting to determine the optimal number of feature maps, were able to find that the reality is not as clear as what other papers tend to suggest. This is not to imply that they are incorrect, but only that there is some uncertainty regarding whether or not a monotonically increasing function best describes the data. As such, it suggests that more research work could be done to dissolve this uncertainty.

It thus appears that the original hypothesis that the generative models would perform significantly better on the occluded task than the discriminative models is not well supported by the results of the experiments performed. Rather, when run in a discriminative manner, the generative model, in our case, the DBN appears to perform close to equally well to the discriminative models, the SVM and the CNN. This suggests that, with regards to other findings in the literature which use generative models and are able to show a difference, that this difference is primarily due to the additional use of reconstruction processes, and is not due to merely the architecture and training algorithm itself.

On the other hand, with regards to DBNs using Gaussian visible units, when trained on the occluded training set and tested on the non-occluded dataset, show remarkable

performance that perhaps warrants further research. In fact, this may suggest that intentionally occluding data sets may allow for good performance on both the non-occluded and occluded tasks, at least when using this particular variant of DBN. Such could prove useful in tasks in which the original training set is non-occluded, but the real-world test data may well be occluded, such as in the case of real-world face recognition from CCTV cameras.

Bibliography

[1] Ackley, D. H., Hinton, G. E. and Sejnowski, T. J. [1985], 'A learning algorithm for boltzmann machines', *Cognitive Science* **9**, 147–169.

[2] Anderson, J. R. [2000], *Cognitive Psychology And Its Implications*, 5th ed. edn, Worth Publishers, New York.

[3] Bengio, Y. [2009], 'Learning deep architectures for ai', *Foundations and Trends in Machine Learning* **2**(1), 1–127.

[4] Bergstra, J., Breuleux, O., Bastien, F., Lamblin, P., Pascanu, R., Desjardins, G., Turian, J., Warde-Farley, D. and Bengio, Y. [2010], Theano: a CPU and GPU math expression compiler, *in* 'Proceedings of the Python for Scientific Computing Conference (SciPy)'.

[5] Boureau, Y.-L., Ponce, J. and LeCun, Y. [2010], A theoretical analysis of feature pooling in visual recognition, *in* 'Proceedings of the 27th International Conference on Machine Learning (ICML-10)', pp. 111–118.

[6] Bryson, A. E. and Ho, Y. C. [1969], *Applied Optimal Control*, Blaisdell, New York.

[7] Chang, C.-C. and Lin, C.-J. [2011], 'LIBSVM: A library for support vector machines', *ACM Transactions on Intelligent Systems and Technology* **2**, 27:1–27:27. Software available at `http://www.csie.ntu.edu.tw/~cjlin/libsvm`.

[8] Chu, J. L. and Krzyżak, A. [2014*a*], Analysis of feature maps selection in supervised learning using convolutional neural networks, *in* M. Sokolova and P. van Beek, eds, 'Canadian Conference on Artificial Intelligence 2014, Lecture Notes on Artifical Intelligece (LNAI)', Vol. 8436, Springer International Publishing Switzerland, pp. 59–70.

[9] Chu, J. L. and Krzyżak, A. [2014*b*], Application of support vector machines, convolutional neural networks and deep belief networks to recognition of partially occluded objects, *in* L. Rutkowski, ed., 'The 13th International Conference on Artificial Intelligence and Soft Computing ICAISC 2014, Lecture Notes on Artifical Intelligece (LNAI)', Vol. 8467, Springer International Publishing Switzerland, pp. 34–46.

[10] Ciresan, D., Meier, U. and Schmidhuber, J. [2012], Multi-column deep neural networks for image classification, *in* 'Proceedings of 2012 IEEE Conference on Computer Vision and Pattern Recognition (CVPR)', IEEE, pp. 3642–3649.

[11] Coates, A., Ng, A. Y. and Lee, H. [2011], An analysis of single-layer networks in unsupervised feature learning, *in* 'International Conference on Artificial Intelligence and Statistics (AISTATS)', pp. 215–223.

[12] Collobert, R. and Bengio, S. [2004], 'Links between perceptrons, mlps and svms', *Proceedings of the 21st International Conference on Machine Learning* p. 23.

[13] Cortes, C. and Vapnik, V. N. [1995], 'Support-vector networks', *Machine Learning* **20**, 273–297.

[14] Dreyfus, S. [1962], 'The numerical solution of variational problems', *Journal of Mathematical Analysis and Applications* **5**(1), 30–45.

[15] Duda, R. O., Hart, P. E. and Stork, D. G. [2001], *Pattern Classification*, second edition edn, John Wiley & Sons, Inc.

[16] Eigen, D., Rolfe, J., Fergus, R. and LeCun, Y. [2013], 'Understanding Deep Architectures using a Recursive Convolutional Network', *ArXiv e-prints* .

[17] Fei-Fei, L., Fergus, R. and Perona, P. [2004], 'Learning generative visual models from few training examples: an incremental bayesian approach tested on 101 object categories', *Workshop on Generative-Model Based Vision, IEEE Computer Vision and Pattern Recognition 2004* .

[18] Fukushima, K. [2003], 'Neocognitron for handwritten digit recognition', *Neurocomputing* **51**, 161–180.

[19] Fukushima, K. and Miyake, S. [1982], 'Neocognitron: A new algorithm for pattern recognition tolerant of deformations and shifts in position', *Pattern Recognition* **15**(6), 455–469.

[20] Hebb, D. [1949], *The Organization of Behaviour*, John Wiley, New York.

[21] Hinton, G. E. [2002], 'Training products of experts by minimizing contrastive divergence', *Neural Computation* **14**(8), 1771–1800.

[22] Hinton, G. E. [2010], 'A practical guide to training restricted boltzmann machines', *Momentum* **9**(1), 599–619.

[23] Hinton, G. E., Osindero, S. and Teh, Y. W. [2006], 'A fast learning algorithm for deep belief nets', *Neural Computation* **18**, 1527–1554.

[24] Hinton, G. E. and Salakhutdinov, R. R. [2006], 'Reducing the dimensionality of data with neural networks', *Science* **313**, 504–507.

[25] Hopfield, J. J. [1982], 'Neural networks and physical systems with emergent collective computational abilities', *Proceedings of the National Academy of Sciences of the USA* **79**(8), 2554–2558.

[26] Huang, F. J. and LeCun, Y. [2006], 'Large-scale learning with svm and convolutional nets for generic object categorization', *Proceedings of the 2006 IEEE Conference on Computer Vision and Pattern Recognition (CVPR)* **1**, 284–291.

[27] Hubel, D. H. and Wiesel, T. N. [1962], 'Receptive fields, binocular interaction and functional architecture in a cats visual cortex', *Journal of Physiology (London)* **160**, 106–154.

[28] Krizhevsky, A., Sutskever, I. and Hinton, G. [2012], Imagenet classification with deep convolutional neural networks, *in* 'Advances in Neural Information Processing Systems 25', pp. 1106–1114.

[29] LeCun, Y., Bottou, L., Bengio, Y. and P., H. [1998], 'Gradient-based learning applied to document recognition', *Proceedings of the IEEE* **86**(11), 2278–2324.

[30] LeCun, Y., Huang, F. and Bottou, L. [2004], 'Learning methods for generic object recognition with invariance to pose and lighting', *Proceedings of IEEE Conference on Computer Vision and Pattern Recognition (CVPR)* **2**, 97–104.

[31] Lee, H., Grosse, R., Ranganath, R. and Ng, A. Y. [2009], 'Convolutional deep belief networks for scalable unsupervised learning of hierarchical representations', *Proceedings of the 26th International Conference on Machine Learning* pp. 609–616.

[32] McClelland, J. and Rumelhart, D. [1988], *Explorations in Parallel Distributed Processing*, MIT Press, Cambridge.

[33] McCulloch, W. S. and Pitts, W. [1943], 'A logical calculus of ideas immanent in nervous activity', *Bulletin of Mathematical Biophysics* **5**, 115–133.

[34] Mehrotra, K., Mohan, C. K. and Ranka, S. [1997], *Elements Of Artificial Neural Networks*, The MIT Press, Cambridge, MA.

[35] Minsky, M. L. and Papert, S. A. [1969], *Perceptrons*, MIT Press, Cambridge.

[36] Mohamed, A. R., Yu, D. and Deng, L. [2010], 'Investigation of full-sequence training of deep belief networks for speech recognition', *Conference of the International Speech Communication Association (INTERSPEECH)* pp. 2846–2849.

[37] Nair, V. and Hinton, G. E. [2009], '3d object recognition with deep belief nets', *Advances in Neural Information Processing Systems (NIPS)* pp. 1339–1347.

[38] Ngiam, J., Chen, Z., Chia, D., Koh, P. W., Le, Q. V. and Ng, A. [2010], 'Tiled convolutional neural networks', *Advances in Neural Information Processing Systems (NIPS)* pp. 1279–1287.

[39] Nguyen, G. H., Phung, S. L. and Bouzerdoum, A. [2009], Reduced training of convolutional neural networks for pedestrian detection, *in* 'International Conference on Information Technology and Applications'.

[40] Osindero, S. and Hinton, G. [2008], 'Modeling image patches with a directed hierarchy of markov random fields', *Advances In Neural Information Processing Systems (NIPS)* **20**.

[41] Pylyshyn, Z. W. [1998], 'What is cognitive science?'.
URL: *http://ruccs.rutgers.edu/ftp/pub/papers/ruccsbook.PDF*

[42] Pylyshyn, Z. W. [2003], 'Return of the mental image: Are there really pictures in the brain?', *Trends in Cognitive Science* **7**(3), 113–118.

[43] Ranzato, M. A., Huang, F. J., Boureau, Y. L. and LeCun, Y. [2007], 'Unsupervised learning of invariant feature hierarchies with applications to object recognition', *2007 IEEE Conference on Computer Vision and Pattern Recognition (CVPR)* pp. 1–8.

[44] Ranzato, M., Susskind, J., Mnih, V. and Hinton, G. [2011], 'On deep generative models with applications to recognition', *2011 IEEE Conference on Computer Vision and Pattern Recognition (CVPR)* pp. 2857–2864.

[45] Rosenblatt, F. [1958], 'The perceptron, a probabilistic model for information storage and organization in the brain', *Psychological Review* **62**, 386–408.

[46] Rumelhart, D. E., Hinton, G. E. and Williams, R. J. [1986], 'Learning internal representations by error propagation', *Parallel Distributed Processing* **1**.

[47] Russell, S. and Norvig, P., eds [2003], *Artificial Intelligence: A Modern Approach*, 2nd ed. edn, Pearson Education, Upper Saddle River, NJ.

[48] Salakhutdinov, R. and Hinton, G. E. [2009], 'Deep boltzmann machines', *International Conference on Artificial Intelligence and Statistics (AISTATS)* pp. 448–455.

[49] Scherer, D., Schulz, H. and Behnke, S. [2010], Accelerating large-scale convolutional neural networks with parallel graphics multiprocessors, *in* 'Artificial Neural Networks–ICANN 2010', Springer, pp. 82–91.

[50] Schulz, H., Muller, A. and S., B. [2010], 'Exploiting local structure in stacked boltzmann machines', *European Symposium on Artificial Neural Networks, Computational Intelligence and Machine Learning (ESANN)* .

[51] Simard, P., Steinkraus, D. and Platt, J. C. [2003], Best practices for convolutional neural networks applied to visual document analysis., *in* 'International Conference on Document Analysis and Recognition (ICDAR)', Vol. 3, pp. 958–962.

[52] Smolensky, P. [1986], Information processing in dynamical systems: Foundations of harmony theory, *in* D. E. Rumelhart and J. L. McLelland, eds, 'Parallel Distributed Processing: Explorations in the Microstructure of Cognition', Vol. 1, MIT Press, chapter 6, pp. 194–281.

[53] Thagard, P. [1996], *Mind: Introduction To Cognitive Science*, The MIT Press, Cambridge, MA.

[54] Uetz, R. and Behnke, S. [2009*a*], Large-scale object recognition with cuda-accelerated hierarchical neural networks, *in* 'IEEE International Conference on Intelligent Computing and Intelligent Systems, 2009. ICIS 2009.', Vol. 1, IEEE, pp. 536–541.

[55] Uetz, R. and Behnke, S. [2009*b*], Locally-connected hierarchical neural networks for gpu-accelerated object recognition, *in* 'NIPS 2009 Workshop on Large-Scale Machine Learning: Parallelism and Massive Datasets'.

[56] Werbos, P. [1974], Beyond regression: New tools for prediction and analysis in the behavioral sciences, PhD thesis, Harvard University.

Appendix A

Original Data of Individual Runs

Comparison of the various models has shown that the occluded problem as implemented in these experiments is an exceedingly challenging one for any machine learning algorithm. Our results with the NORB dataset show this: The SVM trained on the non-occluded set we used was essentially unable to solve the occluded problem at all, achieving results comparable to chance (20%), even though on the non-occluded test set it achieved rates as high as 82%, and on the training data it achieved recognition rates of 99.9%, as seen in table A.1.

Table A.1: The accuracy results of SVMs trained on the non-occluded training set of the NORB dataset.

SVM on NORB - Non-Occluded Training				
Parameters	Accuracy			
	Training	Mixed Test	Non-Occluded Test	Occluded Test
'-g 0.0001 -c 40'	0.982		0.783	0.183
'-g 0.0005 -c 40'	0.999		0.821	0.200
'-g 0.0005 -c 40'	0.999		0.823	0.200
'-g 0.0005 -c 40'	0.999	0.514	0.828	0.200
'-g 0.0005 -c 40'	0.999	0.513	0.827	0.200
'-g 0.0005 -c 40'	0.999	0.510	0.820	0.200
'-g 0.0005 -c 40'	0.999	0.513	0.827	0.200
'-g 0.0005 -c 40'	0.999	0.512	0.823	0.200

When trained exclusively on the occluded training set (see: table A.2), the SVM achieved 94.4% on the training set, 44.6% on the mixed test set, 20% on the non-occluded test set, and 69.2% on the occluded test set. Compared with the 82% achieved on the non-occluded test set by the non-occluded trained SVM, the occluded trained SVM performed more poorly on the occluded test set, but obviously performed better than the non-occluded trained SVM on the occluded test set. Furthermore, it completely failed at classifying the non-occluded images, as 20% for a five class problem is again, basically chance.

Table A.2: The accuracy results of SVMs trained on the occluded training set of the NORB dataset.

SVM on NORB - Occluded Training				
Parameters	Accuracy			
	Training	Mixed Test	Non-Occluded Test	Occluded Test
'-g 0.0005 -c 40'	0.944	0.446	0.200	0.691
'-g 0.0005 -c 40'	0.944	0.446	0.200	0.692
'-g 0.0005 -c 40'	0.944	0.447	0.200	0.693
'-g 0.0005 -c 40'	0.944	0.447	0.200	0.693
'-g 0.0005 -c 40'	0.944	0.446	0.200	0.692

When trained on a mixed training set containing both non-occluded and occluded images, the SVM achieved results that were good across the board, as shown in the third line of table A.3. Notably, the performance on the non-occluded test set was only a couple points lower than the SVMs trained exclusively on the non-occluded training set, while the performance on the occluded test set was actually slightly (within a percentage point) better than the SVMs trained exclusively on the occluded training set.

Table A.3: The accuracy results of SVMs trained on the mixed training set of the NORB dataset.

SVM on NORB - Mixed Training				
Parameters	Accuracy			
	Training	Mixed Test	Non-Occluded Test	Occluded Test
'-g 0.0005 -c 40'	0.973	0.751	0.809	0.693
'-g 0.0005 -c 40'	0.973	0.755	0.815	0.695
'-g 0.0005 -c 40'	0.973	0.755	0.815	0.695
'-g 0.0005 -c 40'	0.973	0.756	0.816	0.696
'-g 0.0005 -c 40'	0.973	0.752	0.810	0.693

The best performing CNN trained exclusively on the non-occluded test set achieved 84% on the non-occluded test set, and 96% on the training data, but only 20%, again at chance with the occluded test set, as seen in table A.4. As the SVM and CNN are discriminative models, these results are somewhat expected.

Table A.4: The accuracy results of CNNs of various parameters on the NORB dataset.

CNN on NORB - Non-Occluded Training													
Parameters		Feature Maps					Learning Step Size		Con Map	Accuracy			
Dataset	Epochs	S1/C2	S3/C4	S5/C6	F7	F8	Start	End		Train	Mixed Test	Non-Occluded	Occluded
	3	12	96	2400	100	5	0.015	0.000338	rand	0.200		0.200	0.200
	3	8	24	24	100	5			rand	0.200		0.200	0.200
	3	8	24	24	100	5			rand	0.200		0.200	0.200
	3	8	24	24	100	5			rand	0.200		0.200	0.200
	3	8	32	128	512	5			rand	0.200		0.200	0.200
24300	3	8	32	128	512	5			rand	0.200		0.200	0.200
1000	3	8	32	128	512	5			rand	0.226		0.247	0.204
1000	3	8	24	24	100	5			rand	0.695		0.506	0.196
1000	3	12	96	2400	100	5			rand	0.200		0.200	0.221
1000	3	8	24	24	100	5			rand	0.759		0.551	0.207
24300	3	8	24	24	100	5			rand	0.601		0.557	0.214
24300	3	8	24	24	100	5	2.00E-05	2.00E-07	rand	0.595		0.553	0.252
24300	10	8	24	24	100	5	2.00E-05	2.02E-07	rand	0.766		0.643	0.240
24300	50	8	24	24	100	5	2.00E-05	1.97E-07	rand	0.896		0.763	0.201
24300	3	8	24	24	100	5	2.00E-05	2.00E-07	full	0.640		0.544	0.177
24300	10	8	24	24	100	5	2.00E-05	2.02E-07	full	0.786		0.703	0.217
24300	50	8	24	24	100	5	2.00E-05	1.97E-07	full	0.902		0.763	0.199
24300	75	8	24	24	100	5	2.00E-05	2.05E-07	rand	0.932		0.802	0.213
24300	100	8	24	24	100	5	2.00E-05	2.1E-07	rand	0.955		0.831	0.199
24300	125	8	24	24	100	5	2.00E-05	1.99E-07	rand	0.962		0.842	0.199
24300	150	8	24	24	100	5	2.00E-05	1.98E-07	rand	0.959		0.825	0.197
24300	100	8	24	24	100	5	2.00E-05	2.1E-07	rand	0.9549	0.515	0.8312	0.199
24300	100	8	24	24	100	5	2.00E-05	2.1E-07	rand	0.955	0.515	0.831	0.199
24300	100	8	24	24	100	5	2.00E-05	2.1E-07	rand	0.955	0.515	0.831	0.199
24300	100	8	24	24	100	5	2.00E-05	2.1E-07	rand	0.955	0.515	0.831	0.199

Note: Dataset indicates how many images from the full dataset were used. Epochs indicates the number of times the network was trained on the training data. Con Map indicates whether the connection map between the higher layers was randomized or fully connected.

The best performing CNN trained exclusively on the occluded test set achieved 69% on the training data, 47% on the mixed test data, 35.2% on the non-occluded test set, and 58.8% on the occluded test set, as seen in table A.5. These results are somewhat interesting, because while the SVM performed at chance on the data set type that it wasn't trained on, the CNN here is performing notably better than chance on the data set type that it wasn't trained on, namely the non-occluded set.

Table A.5: The accuracy results of CNNs trained exclusively on the occluded training set of the NORB dataset.

CNN on NORB - Occluded Training													
Parameters		Feature Maps					Learning Step Size		Con Map	Accuracy			
Dataset	Epochs	S1/C2	S3/C4	S5/C6	F7	F8	Start	End		Train	Mixed Test	Non-Occluded	Occluded
24300	100	8	24	24	100	5	2.00E-05	2.1E-07	rand	0.705	0.424	0.261	0.586
24300	100	8	24	24	100	5	2.00E-05	2.1E-07	rand	0.690	0.470	0.352	0.588
24300	100	8	24	24	100	5	2.00E-05	2.1E-07	rand	0.690	0.470	0.352	0.588
24300	100	8	24	24	100	5	2.00E-05	2.1E-07	rand	0.690	0.388	0.201	0.576
24300	100	8	24	24	100	5	2.00E-05	2.1E-07	rand	0.690	0.470	0.352	0.588

Note: Dataset indicates how many images from the full dataset were used. Epochs indicates the number of times the network was trained on the training data. Con Map indicates whether the connection map between the higher layers was randomized or fully connected.

The CNNs that were trained on a mixed data set as seen in table A.6, showed some-

what lower accuracy on the non-occluded test set than the CNNs trained exclusively on the non-occluded training set, but also showed somewhat higher accuracy on the occluded test set than the CNNs trained exclusively on the occluded training set. It appears that while performance on the non-occluded test set was hampered by mixing in occluded images to the training, the reverse effect occurred with the occluded test set, with performance improved by including non-occluded images.

Table A.6: The accuracy results of CNNs trained on the mixed training set of the NORB dataset.

CNN on NORB - Mixed Training													
Parameters		Feature Maps					Learning Step Size		Con Map	Accuracy			
Dataset	Epochs	S1/C2	S3/C4	S5/C6	F7	F8	Start	End		Train	Mixed Test	Non-Occluded	Occluded
48600	100	8	24	24	100	5	2.00E-05	2.1E-07	rand	0.832	0.719	0.756	0.682
48600	100	8	24	24	100	5	2.00E-05	2.1E-07	rand	0.838	0.708	0.772	0.645
48600	100	8	24	24	100	5	2.00E-05	2.1E-07	rand	0.827	0.723	0.793	0.653
48600	100	8	24	24	100	5	2.00E-05	2.1E-07	rand	0.832	0.719	0.756	0.682

Note: Dataset indicates how many images from the full dataset were used. Epochs indicates the number of times the network was trained on the training data. Con Map indicates whether the connection map between the higher layers was randomized or fully connected.

What was interesting was the performance of our generative models on the occluded problem. The best DBN, again trained on the non-occluded training set, achieved 86% accuracy on the non-occluded test set, and 99.4% accuracy on the training data, but only achieved 22.2% accuracy on the occluded test set, which was only slightly better than chance (shown in table A.7). Note that a DBN using Gaussian visible units was able to achieve slightly better results at 25.6% accuracy on the occluded test set, albeit at a cost to performance on the non-occluded test set, which it achieved only 80% on. While these results are low, they are at least somewhat better than the discriminative models.

Table A.7: The results of DBNs of various parameters trained on the non-occluded training set on the NORB dataset.

DBN on NORB - Non-Occluded Training												
Visible	Parameters		Learning Rate		Epochs		Accuracy			Fine-Tuned Accuracy		
	Layers	Hidden	RBM	Fine-Tune	RBM	Fine-Tune	Training	Non-Occluded	Occluded	Training	Non-Occluded	Occluded
Gaussian	2	2000	0.001	0.001	200	50	0.531	0.465	0.241	0.986	0.802	0.256
Binary	2	2000	0.100	0.010	200	50	0.200	0.200	0.200	0.200	0.200	0.200
Binary	2	2000	0.010	0.001	200	50	0.622	0.559	0.226	0.993	0.860	0.222
Gaussian	2	4000	0.001	0.001	200	50	0.522	0.461	0.249	0.977	0.837	0.233
Binary	2	4000	0.010	0.001	200	50	0.611	0.535	0.239	0.990	0.859	0.201

Note: Visible indicates the type of visible input nodes. Layers indicates the number of RBMs. Hidden indicates the number of hidden nodes in the hidden layer of each RBM.

More interesting perhaps were the results of training the DBN on just the occluded training dataset. The results (shown in table A.8) are interesting because while the binary visible unit based DBNs perform as expected, with much higher performance on the oc-

cluded test set (72.2%) than the non-occluded test set (27.8%), the Gaussian visible unit based DBNs have the unusual property of performing reasonably well on both the non-occluded (70.0%) and occluded (64.4%) test sets. Why these Gaussian visible unit based DBNs, trained only on the occluded images, performed so well on the non-occluded images is unknown and perhaps worth further investigation.

Table A.8: The results of DBNs of various parameters trained on the occluded training set on the NORB dataset.

DBN on NORB - Occluded Training												
Visible	Parameters		Learning Rate		Accuracy				Fine-Tuned Accuracy			
	Layers	Hidden	DBN	Fine-Tune	Training	Test	Non-Occluded	Occluded	Training	Test	Non-Occluded	Occluded
Binary	2	2000	0.010	0.001	0.513	0.350	0.230	0.458	0.858	0.500	0.278	0.722
Binary	2	4000	0.010	0.001	0.459	0.318	0.206	0.428	0.846	0.466	0.220	0.712
Gaussian	2	4000	0.001	0.001	0.327	0.266	0.233	0.301	0.787	0.672	0.700	0.644

Note: Visible indicates the type of visible input nodes. Layers indicates the number of RBMs. Hidden indicates the number of hidden nodes in the hidden layer of each RBM.

Also interesting was the performance of the DBN when trained on a mixed dataset including both non-occluded and occluded images as seen in table A.9. Though the performance on the non-occluded test set is somewhat lower (at best 80.7%) than when trained just on the non-occluded training set, the performance on the occluded test set is significantly better, around 68-69%. The performance on the mixed test set combining both non-occluded and occluded test sets is at best 74.4%.

Table A.9: The results of DBNs of various parameters trained on the mixed training set on the NORB dataset.

DBN on NORB - Mixed Training												
Visible	Parameters		Learning Rate		Accuracy				Fine-Tuned Accuracy			
	Layers	Hidden	DBN	Fine-Tune	Training	Mixed	Non-Occluded	Occluded	Training	Mixed	Non-Occluded	Occluded
Binary	2	2000	0.010	0.001	0.542	0.477	0.514	0.439	0.821	0.654	0.618	0.697
Binary	2	4000	0.010	0.001	0.510	0.446	0.482	0.413	0.881	0.672	0.658	0.686
Gaussian	2	4000	0.001	0.001	0.401	0.366	0.443	0.298	0.898	0.744	0.807	0.680

Note: Visible indicates the type of visible input nodes. Layers indicates the number of RBMs. Hidden indicates the number of hidden nodes in the hidden layer of each RBM.